

**MASTER**

**Plasma electrolytic oxidation for catalyst and membrane applications**

Venkat Prahlad, A.

*Award date:*  
2021

[Link to publication](#)

**Disclaimer**

This document contains a student thesis (bachelor's or master's), as authored by a student at Eindhoven University of Technology. Student theses are made available in the TU/e repository upon obtaining the required degree. The grade received is not published on the document as presented in the repository. The required complexity or quality of research of student theses may vary by program, and the required minimum study period may vary in duration.

**General rights**

Copyright and moral rights for the publications made accessible in the public portal are retained by the authors and/or other copyright owners and it is a condition of accessing publications that users recognise and abide by the legal requirements associated with these rights.

- Users may download and print one copy of any publication from the public portal for the purpose of private study or research.
- You may not further distribute the material or use it for any profit-making activity or commercial gain



Eindhoven University of Technology  
Department of Chemical Engineering and Chemistry

# **Plasma electrolytic oxidation for catalyst and membrane applications**

*Master Thesis*

Anirudh Venkat Prahlad  
1383116

Supervisors:  
Prof. dr. Eng. Fausto Gallucci  
Dr. ir. Hamid Reza Godini  
Dr. Sirui Li

Eindhoven, March 2021

## Abstract

Plasma electrolytic oxidation (PEO) is an increasingly used surface modification technique to produce thick, ceramic oxide coatings on the surface of a metal or metal alloy. The attractiveness of this technique stems from the fact that the produced coatings can be tailored and customized to a very large extent. The flexibility in the process can be attributed to variation in process parameters such as applied voltage, applied current, frequency and electrolyte type and concentration.

This work explores the utilization of PEO as base for catalyst and membrane applications. Titanium was considered as a suitable material for this work owing to its high melting point, hardness and strong affinity to oxidation. Different titanium samples such as discs, wires, porous tubes and 3D printed titanium scaffolds were processed by PEO. The applied voltage, frequency and electrolyte concentration were varied to obtain titania ( $\text{TiO}_2$ ) coatings with different morphologies and compositions. In addition to titanium, zirconium wires were also processed by variation of the same process parameters. All the experimentation was performed by application of a constant voltage (Potentiostatic mode).

Characterization techniques like SEM-EDX and XRD were used to determine the coatings structure, elemental and phase composition. All samples possessed crater like structures on their surface which is characteristic of a PEO process. The SEM-EDX and XRD data, combined with visual observation of spark discharge on the sample surface during processing confirmed that the samples had been successfully oxidized by PEO.

The extent of oxidation was shown to increase with increasing applied voltage and electrolyte concentration. In addition, increase in these parameters resulted in increased electrolyte component deposition on the coatings

All the samples except for the porous tubes showed the presence of anatase which is one of the crystalline phases of  $\text{TiO}_2$ . This is desired as the catalytic and membrane applications operate at moderate (150 – 300 °C) to high (850 °C) temperatures, and crystallinity in the coatings increase its thermal resistance.

It was determined that the wire samples were a viable choice for use as a support for catalyst applications owing to their small surface area, availability and easy workability. The flexibility in customizing the coating characteristics is another reason why these samples can be used as a support for catalyst impregnation.

The tube samples showed spark discharge but the oxide layer did not contain anatase  $\text{TiO}_2$ . Therefore, further research and experimentation is warranted for use of the tubes in membrane applications.

## Acknowledgements

I would like to express my sincere gratitude to my direct supervisors Dr.ir Hamid Godini and Dr. Sirui Li for their invaluable advice, support and guidance throughout the course of this project. Despite their busy and packed schedules, they always made time to answer any doubts or clarification that I may have had. I would also like to further thank Dr. Hamid Godini for being by my side all through the duration of this project and for checking up on me and reminding me to complete certain tasks from time to time to keep me in track. His dedication and commitment to this project is noteworthy and inspiring to me.

I would also like to sincerely thank Dr.ing. Oliver Görke at Technische Universität Berlin for performing XRD on a number of our samples. In addition, I would also like to thank Dr. Vesna Middelkoop at VITO for providing us with the 3D printed scaffold supports that were used in our experimentation.

I would also like to thank Prof. Fausto Gallucci, my graduate supervisor for his advice and guidance and making time for me despite his very busy schedule. His technical advice and guidance on certain concepts of this work were extremely useful and helpful. Furthermore, his ever-helpful nature regarding the financial aspect of this work ensured that there were no major roadblocks and I would like to further express my gratitude to him for that support.

Last but not least, I would like to thank my family and friends for helping and staying by me through this extremely busy and hectic time. The unconditional love and support that they showed me is highly appreciated.

# Contents

Abstract	i
Acknowledgements	ii
List of figures	v
List of tables	viii
Nomenclature	ix
1. Introduction	1
1.1. Background	1
1.2. Comparison between Plasma electrolytic oxidation and conventional DC anodizing	2
1.3. Aim of this study	3
1.4. Porous metal membranes	3
1.5. Oxidative coupling of methane in catalytic membrane reactors	5
2. Theory	7
2.1. Experimental setup for plasma electrolytic oxidation	7
2.2. Surface pre-treatment of titanium and establishing electrical connections	8
2.3. Influence of electrical parameters on the PEO process	9
2.3.1. Influence of the electrolyte	9
2.3.2. Influence of current density	10
2.3.3. Influence of duty cycle and frequency	11
2.4. Thermal stability of oxide coatings of titanium and its alloys at high temperatures	11
2.4.1. Titanium alloy (Ti6Al4V)	11
2.4.2. Pure titanium	12
2.5. Plasma electrolytic oxidation on porous titanium	12
2.6. Tuning the thickness and pore size of the coatings	12
2.7. Coating phases of titania formed by plasma electrolytic oxidation	13
2.8. Plasma electrolytic oxidation on titanium foams	13
2.9. Plasma electrolytic oxidation on 3D printed titanium scaffolds	14
2.10. Plasma electrolytic oxidation on tubular samples	15
2.11. Plasma electrolytic oxidation on non-valve metals	16
2.12. Plasma electrolytic oxidation on steel	17
3. Materials and methods	19
3.1. Experimental setup and samples processed	19
3.2. Variation of process parameters	24

3.3.	Material characterization	24
3.3.1.	Surface morphology	24
3.3.2.	Element identification and phase composition	25
3.4.	Current-time data	25
4.	Results and discussion	26
4.1.	Plasma discharge phenomena and equivalent circuit diagrams	26
4.2.	Current-time data	28
4.3.	SEM-EDX	38
4.4.	XRD	46
4.5.	Comparison between coated and non-coated samples	50
4.6.	Coating thickness	53
4.7.	Electrolyte temperature	54
5.	Conclusions	56
6.	Recommendations for future work	58
7.	References	59

## List of figures

Figure 1-1 Conceptual design for the reactor description in the project	5
Figure 2-1 Main components required for Plasma electrolytic oxidation	7
Figure 2-2 Equipment used in a Plasma electrolytic oxidation coating setup	7
Figure 2-3 Connections for rectangular and circular (disc) workpieces	9
Figure 2-4 Crocodile-clip connection for larger workpieces	9
Figure 2-5 Structure and dimension of the 3D printed scaffold samples	14
Figure 2-6 Experimental setup to coat tubular structures. (1) electrolytic bath (2) voltage probes (3) stainless steel cathode (4) surface of the electrolyte (5) tube to be coated (6) central accessory electrode	15
Figure 2-7 Voltage drop without using the central accessory electrode	16
Figure 2-8 Voltage drop when using the central accessory electrode	16
Figure 2-9 Free energy of formation for various oxides	17
Figure 3-1 Experimental setup used for PEO where; A) cooler B) Magnetic stirrer C) counter electrode D) electrolytic bath E) workpiece being coated	19
Figure 3-2 Electrical connection for the 1 and 1.5 cm diameter titanium disc samples	20
Figure 3-3 Connections for left) three titanium wires; right) titanium wire bundle	21
Figure 3-4 Visualisation of the 3D printed titanium scaffold left) front view; right) top view	22
Figure 3-5 Wound 3D printed titanium scaffold sample	22
Figure 3-6 Porous titanium tube	23
Figure 3-7 Connection for the 1 cm long porous titanium tube sample	23
Figure 4-1 Spark discharge observed on left) single titanium wire; right) three titanium wire sample	26
Figure 4-2 Seizing of spark discharge on the titanium wire samples	27
Figure 4-3 Equivalent circuit diagram representing the electrical system	27
Figure 4-4 Current time graph for a 1 cm diameter titanium disc sample processed with the aluminate based electrolyte (E1) at 50 Hz	28
Figure 4-5 Effect of electrolyte composition for disc samples processed in the silicate based electrolyte	29
Figure 4-6 Effect of frequency A) 50 Hz; B) 200 Hz for 1 cm disc samples in the silicate based electrolyte	30
Figure 4-7 Effect of voltage for disc samples in the silicate based electrolyte	31
Figure 4-8 Effect of voltage for disc samples in the aluminate based electrolyte	31
Figure 4-9 Current time data for partially immersed 3D printed scaffold samples	32

Figure 4-10 Current time data for 3D scaffold samples wound with titanium wire and processed in the aluminate based electrolyte	33
Figure 4-11 Current-time graphs for titanium wire samples for the variation of A) electrolyte concentration; B) frequency; C) voltage in the silicate based electrolyte	34
Figure 4-12 Current-time graphs for titanium wire samples for the variation of A) electrolyte concentration; B) voltage; C) frequency in the aluminate based electrolyte	35
Figure 4-13 Current time data for a titanium wire bundle sample	36
Figure 4-14 Current time data for Zr wire samples containing three wires in the aluminate based electrolyte, for the effect on A) voltage; B) electrolyte concentration	37
Figure 4-15 Current time graph for a Zr wire bundle sample with voltage ramps	38
Figure 4-16 SEM-EDX for 1 cm disc (200 V, 200 Hz, Na <sub>2</sub> SiO <sub>3</sub> , E3)	38
Figure 4-17 SEM-EDX for 1 cm disc (200 V, 200 Hz, Na <sub>2</sub> SiO <sub>3</sub> , E2)	38
<i>Figure 4-18 SEM-EDX for 1 cm disc (230 V, 50 Hz, Na<sub>2</sub>SiO<sub>3</sub>, E1)</i>	39
Figure 4-19 SEM-EDX for 1 cm disc (230 V, 50 Hz, Na <sub>2</sub> SiO <sub>3</sub> , E2)	39
Figure 4-20 SEM-EDX for 1 cm disc (230 V, 50 Hz, Na <sub>2</sub> SiO <sub>3</sub> , E3) - dense	39
Figure 4-21 SEM-EDX for 1cm disc (230 V, 50 Hz, Na <sub>2</sub> SiO <sub>3</sub> , E3) - porous	39
Figure 4-22 SEM-EDX for a cut 3D scaffold sample (200 V, 50 Hz, Na <sub>2</sub> SiO <sub>3</sub> , E1) for two different regions A and B on the same sample	41
Figure 4-23 SEM images of a 3D printed scaffold A) lateral surface (20x); B) top view of the struts (185x); C) Top view (280x); D) Structure of a single strut (1200x); E) particle structure (6700x)	42
Figure 4-24 SEM-EDX of 1 cm long porous Ti tubes (200 V, 50 Hz, NaAlO <sub>2</sub> , E1) for two regions A) and B) of the same sample	42
Figure 4-25 SEM-EDX for TW wire samples (50 Hz, NaAlO <sub>2</sub> , E2) at A) 220 Volts; B) 240 Volts; C) 260 Volts	43
Figure 4-26 SEM images at different regions and magnifications of a TW sample (260 V, 200 Hz, NaAlO <sub>2</sub> , E3)	44
Figure 4-27 SEM-EDX for Zr wire samples A) and B) (220 V, 50 Hz, NaAlO <sub>2</sub> , E2); C) and D) (240 V, 50 Hz, NaAlO <sub>2</sub> , E2)	45
Figure 4-28 SEM-EDX for Zr wire bundle sample (200 V, 50 Hz, Na <sub>2</sub> SiO <sub>3</sub> , E1)	46
Figure 4-29 XRD for 1 cm diameter titanium disc samples	47
Figure 4-30 XRD for 1 cm long porous tubular samples	47
Figure 4-31 XRD for 3D printed titanium scaffold	48
Figure 4-32 XRD for titanium wire bundle samples	49
Figure 4-33 XRD for zirconium wire bundle samples	49



Figure 4-34 SEM-EDX for left) Uncoated; right) Coated 1 cm porous titanium tube sample	51
Figure 4-35 SEM-EDX for left) Uncoated; right) Coated 3D printed titanium scaffold	51
Figure 4-36 SEM-EDX for left) Uncoated; right) Coated titanium wire sample	52
Figure 4-37 SEM-EDX for left) Uncoated; right) Coated zirconium wire sample	52
Figure 4-38 SEM-EDX for left) Uncoated; right) Coated 1 cm diameter titanium disc sample	53
Figure 4-39 Cross sectional SEM image of a coated titanium wire sample	54
Figure 4-40 Electrolyte temperature measured before and after an experimental run	55

## List of tables

Table 1-1 Comparison between conventional direct current anodizing and plasma electrolytic oxidation	2
Table 1-2 Various fabrication techniques used for porous metal frameworks with different pore size ranges	4
Table 3-1 Details of the porous titanium tubes	23
Table 3-2 Electrolyte details	24

## Nomenclature

---

<b>SEM</b>	Scanning electron microscopy	
<b>EDX</b>	Energy-Dispersive X ray spectroscopy	
<b>XRD</b>	X – Ray diffraction	
<b>PEO</b>	Plasma electrolytic oxidation	
<b>TW/TWB</b>	Titanium wire/Titanium wire bundle	
<b>ZW/ZWB</b>	Zirconium wire/Zirconium wire bundle	
<b>OCM</b>	Oxidative coupling of methane	
<b>tm</b>	Sparking time or time at which the maximum current is reached	[s]
<b>Am</b>	Sparking current or maximum current	[A]

---

# 1. Introduction

## 1.1. Background

Plasma electrolytic oxidation (PEO) is an increasingly applied surface modification technique to produce thick, ceramic oxide layers on the surfaces of metals and metal alloys. Its functioning is largely similar to that of anodization where a potential is applied between two electrodes to generate an oxide layer on the workpiece that is to be coated (section 1.2). The differentiating factor is the applied voltage and currents which is higher than the dielectric breakdown potential of the workpiece being coated. As a result, spark discharge is observed all over the sample's surface. This sparking is preceded by the formation of gas bubbles at the vicinity of the sample surface which act as paths or channels for current to flow, thereby resulting in the formation and growth of the oxide coating layer.

PEO can be used to grow thick, crystalline coatings on metals such as titanium, aluminum and magnesium. These coatings offer protection against wear and tear, corrosion, heat as well as electrical insulation as they possess high hardness and form a continuous passivating barrier over the surface of the workpiece. The crystallinity of the coatings can be attributed the high localized temperatures and pressures arising from the plasma discharge.

Since the oxide coating is formed as a result of conversion of the substrate into its oxide, it grows both inwards and outwards from the metal surface resulting in the formation of strongly adherent coatings to the surface of the workpiece. PEO coatings in general are shown to possess a tri-layered structure [1]. The layer that is adhered to the workpiece surface is the inner dense layer which is the thinnest of the three layers and possess the highest microhardness. Above this layer, is the transition layer which is less dense than the inner layer but is more porous due the presence of electrolyte deposited compounds. The third layer is the outer most porous layer that accounts for majority of the coating thickness. It is in this layer that a majority of the electrolyte deposition takes place. The morphology and structure of the coatings are influenced by the process parameters used, which are primarily either voltage or current, frequency in case an alternating current (AC) is used and the electrolyte type and composition. It is due to these factors that the PEO process is known to provide a lot of flexibility and potential to tune the coating characteristics based on the requirement [2-3]. Due to these qualities, PEO can be utilized for membrane applications [4], as well as to form support layers for catalyst impregnation which can later be used in catalytic reactor systems. Conventionally, membranes have been fabricated in many ways. One such method being by dip coating followed by calcination [5] where a  $\alpha$ -Al<sub>2</sub>O<sub>3</sub> membrane is modified by dipping in a glassy compound like BOTZ. This is done to tailor the pore size of the outer membrane layer to facilitate more efficient diffusion of gasses through the membrane. The membrane applications for which PEO will be utilized are oxidative

coupling of methane (OCM) and CO<sub>2</sub> utilization. OCM is a high temperature gas separation application which the reactions take place at 850 °C and higher. Hence, it is critical to use materials and membranes that have the thermal stability to withstand those temperatures. Based on the pore size and porosity of the membranes, they can be classified into porous or dense membranes [6]. Both have been used before for OCM and the membranes employed are largely inorganic owing to the high temperature requirement. Conventional polymer or organic membranes would not be able to operate at the temperatures required for OCM or CO<sub>2</sub> utilization [7].

The motivation for using PEO as a technique for membrane modification is that base metal can be directly coated by a thick, ceramic passivating layer of its own metal oxide. As mentioned before, the oxide coatings can further be modified to tailor the porosity, hardness and pore size of the coated layer by varying the process parameters. In addition, electrolyte components can be incorporated into the coating based on the type and composition of the electrolyte used.

The second application of PEO in this work is for catalyst applications. Due to the customizability that PEO offers in tailoring the coating characteristics, it serves as a strong choice as a support layer for catalyst impregnation.

## 1.2. Comparison between Plasma electrolytic oxidation and conventional DC anodizing

The primary reason behind applying coatings and finishing techniques to the surface of metals is to improve their characteristics such as include corrosion resistance, wear resistance, heat resistance, etc. Numerous such surface modification techniques are present, such as conversion coatings, metallic coatings and powder coatings.

The electrochemical process by which coatings are conventionally applied to metals anodizing. This technique involves the use of an electrolyte in which the metal substrate to be coated is immersed. A thin oxide film is produced on the surface on passing a voltage through the electrolyte, between the counter electrode and workpiece. Anodizing has been used as the conventional coating process due to its reliability and ease of operation. PEO can be looked at as a modification to the conventional anodizing process in terms of its applied process conditions. These differences are outlined in Table 1-1 [8]

*Table 1-1 Comparison between conventional direct current anodizing and plasma electrolytic oxidation [8]*

<b>Property</b>	<b>Conventional DC anodizing</b>	<b>Plasma electrolytic oxidation</b>
Cell voltage (V)	20 - 80	120 and above
Current density (A/dm <sup>2</sup> )	<10	<30
Substrate pre-treatment	Critical	Less critical

Common electrolytes	Sulphuric or phosphoric acids	Neutral or alkaline pH 7 - 12
Ability to coat alloys containing intermettals	Relatively poor	Improved
Oxide thickness ( $\mu\text{m}$ )	<10	<200
Hardness	Moderate	Relatively high
Adhesion to substrate	Moderate	Very high
Temperature control	Critical	Not very important

---

### 1.3. Aim of this study

The possibility of using PEO as a surface modification technique for membrane and catalyst applications is studied. A literature review of PEO is first performed to determine if such a technique has been used in the past to fabricate porous metal membranes. Following which, materials and equipment are selected based on the electric parameter requirements to coat the selected samples. Initially, to better understand the process, it is important to coat samples that are readily available and which are the same material as that of the porous membrane that will be used as a base for the membrane application. The initial processed samples act as a control to determine and understand the behavior and discharge characteristics of PEO on that metal. It is not only important to form coatings on the metal surface but also ensure that they possess desired characteristics such as thickness, porosity, pore size and also crystallinity. The coated samples will be characterized by techniques such as SEM, EDX and XRD to determine their surface morphology, elemental composition and phase composition.

Process parameters such as applied voltage, frequency and electrolyte composition are varied to determine their effect on the coating characteristics. The knowledge of the effect of the process parameters coupled with SEM, EDX and XRD data would give an indication of how the process parameters can be varied to further tune the oxide coatings characteristics to obtain desired coatings for use in both catalyst and membrane application.

### 1.4. Porous metal membranes

Inorganic membranes are those which are prepared from materials such as silica, zeolite, oxides (for example  $\text{Al}_2\text{O}_3$ ,  $\text{TiO}_2$ ) and metals such as Pd, Al, alloys and steel [9]. They find particular interest in membrane separation applications due to their long operational lifetimes, high chemical, thermal and mechanical stresses and good separation features. The other type of membranes that are widely used in the industry today for low temperature separation application are the polymeric or organic membranes. Most of the metal membranes are composed of a similar composite structure in which

there is a metal base and a metal oxide or alloy separation layer. They are broadly classified into dense and porous metal membranes. The main focus being on porous metal membranes [9] as it is relevant to the scope of this work. Porous metal membranes in general can be further be classified into two distinct categories which are supported and unsupported membranes. Unsupported metal membranes are composed of pure or alloyed metals and supported membranes are composed of a porous metal as the primary structure with a metal alloy or oxide which acts a membrane selective layer. The porous metal membrane's morphology such as pore size, depth and porosity are heavily dependent on their fabrication method. Table 1-2 shows the various fabrication processes that have used on the base metal frameworks and their achievable pore sizes [9].

*Table 1-2 Various fabrication techniques used for porous metal frameworks with different pore size ranges [9]*

Pore Size	Techniques	Advantages	Disadvantages
>100 $\mu\text{m}$	Casting [9,22]	Close control of the pore size distribution.	Inadequate interconnectivity of the pores.
	Electroplating [22,23]	High efficiency for the fast processing of rough metal coatings.	Required to use the surface as an electrode, which leads to pore filling and clogging within porous structures, thus substantially reducing the surface porosity and pore density.
	Chemical vapour deposition (CVD) [9,24–26]	Can produce a thin imprint that accurately follows the topography and morphology of the substrate.	Usually only used to coat thin layers of pure metals onto the substrate.
1–100 $\mu\text{m}$	Thermal sintering [27–32]	Mature technology, easily scale up, cheap to process.	Low pore connectivity and limited porosity.
50 nm–1 $\mu\text{m}$	Template-directed synthesis [33,34]	Can deposit metals onto a template structure of the desired pore size (e.g., colloidal arrays).	The uniform deposition of metals into colloidal arrays is challenging.
	De-alloying [8,35–39]	Could lead to very homogeneous structures with narrow pore size distribution.	Difficult to form ultra-thin films of fine grain size alloys.
	Electro-spinning [40–46]	High up-scalability and low cost.	Mechanical strength needs to be enhanced by post-treatments.
	Wet casting/coating [47–49]	Easy to implement.	Relatively large pores (~1 $\mu\text{m}$ ) may exist in the final membranes.
	Ink-jet printing [50–59]	Cost effective, form multi-material components, precisely fabricate intricate layers, able to cover 3D surfaces.	Need post-treatments, still immature.
	Electrical sintering [60,61]	Creates finer structures than thermal sintering.	Only can achieve very thin films (<250 nm).
1 nm–50 nm	Electroless deposition [62–67]	Highly controllable structures with nano-scale pore distribution, able to simultaneously co-deposit multiple metals.	Very low deposition rate, a careful analytical control of the plating bath is required, high cost.
	Block co-polymer (BCP) [68–71]	Fine control of the nanoparticle distribution, can result in highly crystallised and ordered structures.	Using expensive BCPs prohibits their expansion to a large scale.

Despite the numerous fabrication techniques that are possible, one of the main approaches is that of particle sintering. In this process, the particles coalesce to form necks at high temperatures when the metal is relatively soft. The most common metal used for fabrication of porous metal membranes is stainless steel (SS) but other metals such as gold, copper, silver, nickel, etc. can be used as well [10]. Supported porous metal membranes are usually fabricated by coating a thin oxide layer on the metal surface which acts as a membrane selective and passivating layer. Plasma electrolytic oxidation can be used as an alternate fabrication method to produce composite porous metal membrane structures, with the base being the metal itself and the oxide layer acting as the membrane selective layer. This

is also why the aim of this study is to try and coat an oxide layer on a porous titanium support, thereby forming a composite membrane structure.

## 1.5. Oxidative coupling of methane in catalytic membrane reactors

Oxidative coupling methane (OCM) is an example of a partial oxidation reaction in which oxygen is added to methane in a controlled manner to produce hydrocarbons such as ethane and subsequently ethylene which is the desired product. It is known that the intermediate products tend to react more vigorously with oxygen. Therefore, a controlled addition of oxygen to methane is required to prevent excessive oxidation [11]. This process is usually carried out in a membrane reactor which is equipped with a distributor membrane. Oxygen is allowed to permeate through the membrane and react with methane to facilitate the OCM reaction. For satisfactory permeability of reactions involving methane, the reaction temperatures are above 700 °C [11].

There are different reactor configurations that are possible for membrane reactors. Three of which are discussed in [6]

- a) Packed bed reactor where the tube containing the catalyst is a porous membrane
- b) Dense membrane reactor
- c) Membrane reactor with the catalyst embedded within the membrane pores.

The first reactor configuration is focused on as that is the reactor setup that was proposed to be used after fabrication of the PEO coated titanium membranes which is related to the scope of this study. Furthermore, this configuration allows for the controlled release of oxygen through the membrane which is of high importance in OCM.

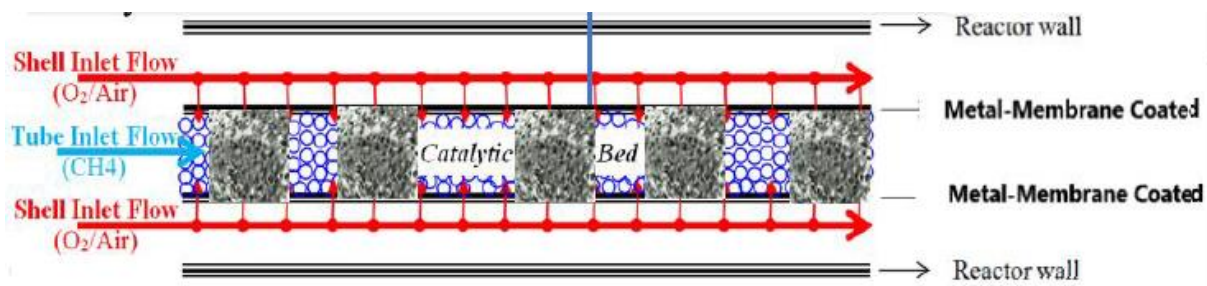


Figure 1-1 Conceptual design for the reactor description in the project

A comprehensive study of OCM was performed in [6] for inorganic catalytic membrane reactors using various membranes and catalysts. In the case of a packed bed reactor setup with a tube fit with a membrane and filled with catalyst particles, two types of membrane materials were studied. The most common porous membranes for OCM was found to be  $\alpha$ -alumina and zirconia, but  $\alpha$ -alumina is more widely used. A suitable catalyst for the process was found to be Samarium oxide ( $\text{Sm}_2\text{O}_3$ ) which was due to the fact that it showed almost no deactivation and loss of selectivity, even after 100 hours of



operation. The  $\alpha\text{-Al}_2\text{O}_3$  membrane was shown to be able to withstand the high temperatures required for OCM, which is greater than 750 °C.

## 2. Theory

### 2.1. Experimental setup for plasma electrolytic oxidation

The components necessary to perform plasma electrolytic oxidation are shown in figure 2-1. It is becoming increasingly common to use AC power sources for PEO due to better control over the process and formation of better-quality coatings [8].

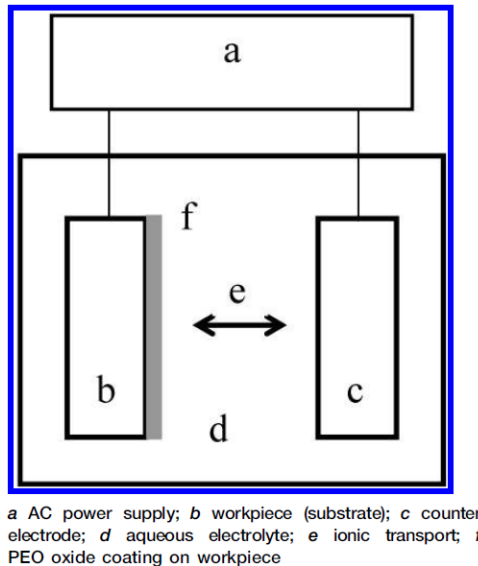


Figure 2-1 Main components required for Plasma electrolytic oxidation [8]

A complete experimental setup which can be used to conduct experimentation on PEO is shown in figure 2-2.

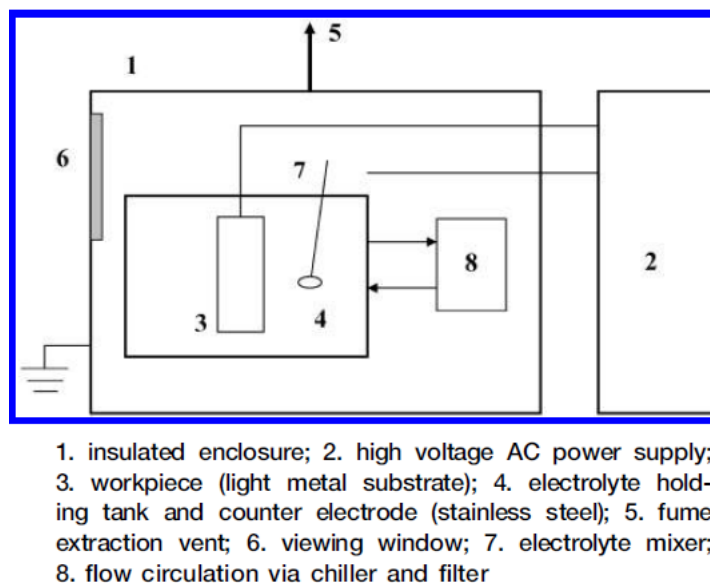


Figure 2-2 Equipment used in a Plasma electrolytic oxidation coating setup [8]

It can be seen that the setup where the process takes place is situated within an insulated enclosure (1). The insulated enclosure is placed close to a high voltage AC power source (2) so that the electrical

connections can be easily established with the electrodes. The metal workpiece (3) which is to be coated by PEO is immersed in an electrolyte which is present in an electrolyte holding tank or bath (4). The electrolyte bath can also serve as a counter electrode. It is insulated and usually made of stainless steel due to its higher corrosion resistance compared to mild steel or standard carbon steel. The setup is also equipped with a fume extraction vent (5) to safely vent fumes produced during the process to the atmosphere. A viewing window (6) is also present on the enclosure to safely observe the process. In order to ensure uniform composition and homogeneity of the electrolyte, the electrolyte tank should be fitted with a mixer (7). The electrolyte in the tank is circulated by a flow circuit which contains a chiller or a heat exchanger (8) with a filter.

## 2.2. Surface pre-treatment of titanium and establishing electrical connections

Titanium is a noble metal which means that it has a natural tendency to form a thin passivating oxide layer on its surface at room temperatures. Surface pretreatment on titanium can be performed by immersing the workpiece in a dilute solution of nitric acid ( $\text{HNO}_3$ ) and hydrofluoric acid (HF) for 30 seconds. This dissolves the natural oxide layer and might even remove some of the surface contaminants on the workpiece as well [12].

In [13], pre-treatment of the workpiece was done by (1) Polishing the metal with SiC abrasive paper, (2) Degreasing the workpiece by immersion in acetone for ten minutes. Finally, (3) cleaning was done by immersion in a solution of HF (3%)/ $\text{HNO}_3$  (30%) to remove the naturally formed oxide layer, if present. In certain cases, coating samples with a large surface area by PEO might not be possible due to the large power and current requirement. Therefore, to control the working surface area of samples, the surface of the workpiece can be coated with lacquer (Stopper 45 MacDermid) [14].

### **Establishing electrical connections to the work-piece**

In most cases, electrical contact is made by drilling a threaded hole into the side of the sample [15]. A steel rod insulated by a ceramic is then bolted to the samples through the threaded hole and connected to the power source forming the electrical contact.

Such type of connections can be seen in figure 2-3, where rectangular and disc samples were coated. The advantage of using such a connection is that the entire workpiece can be immersed in the electrolyte which would result in its entire surface area being exposed to oxidation by PEO.

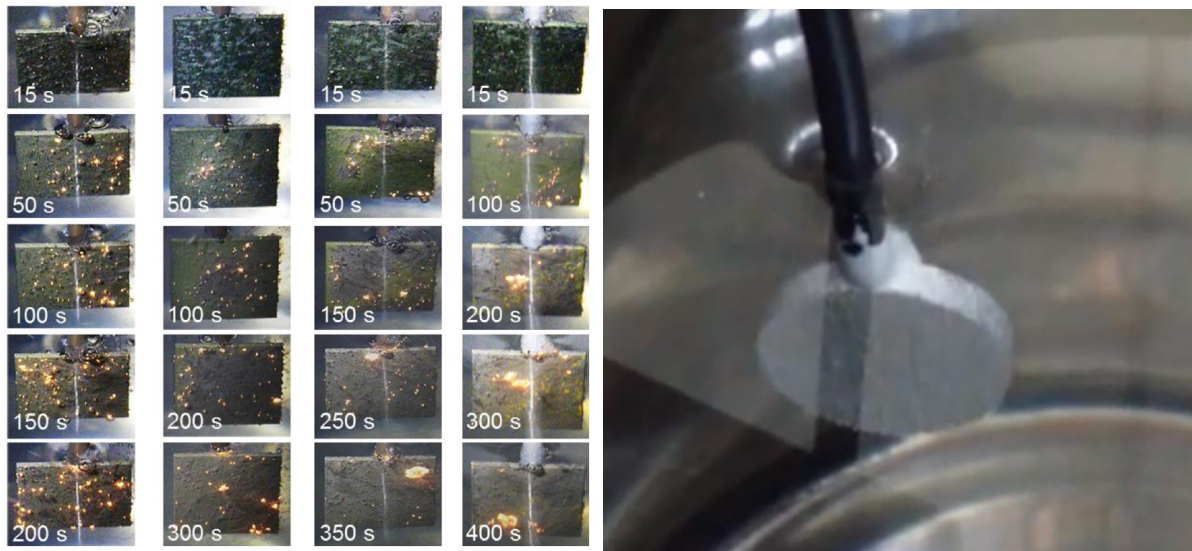


Figure 2-3 Connections for rectangular and circular (disc) workpieces

If the workpiece is relatively large in size, it can be connected by means of a crocodile clip connection as seen in figure 2-4. The only drawback on this type of connection is that a portion of the workpiece will remain above the surface of the electrolyte and will not be coated.



Figure 2-4 Crocodile-clip connection for larger workpieces

## 2.3. Influence of electrical parameters on the PEO process

### 2.3.1. Influence of the electrolyte

#### a) Using a silicate based electrolyte

In [16], PEO coatings were formed on pure titanium in a silicate based electrolyte containing 0.5 M (20 g/l) NaOH and sodium metasilicate ( $\text{Na}_2\text{SiO}_3$ ) in concentrations of 0 – 0.16 M (0 - 19.526 g/l). A pulsed DC mode was used along with a duty cycle of 30% and an oxidation time of five minutes. It was found that the electrolyte containing 0.16 M  $\text{Na}_2\text{SiO}_3$  showed the most homogeneous pore structure with the largest pores being 2  $\mu\text{m}$ . On increasing the concentration of  $\text{Na}_2\text{SiO}_3$ , the conductivity of the

electrolyte increased, resulting in larger pores being formed due to the occurrence of more concentrated and intense plasma discharges.

#### **b) Effect of cerium oxide additive**

The effect of current density and concentration of Cerium oxide ( $\text{CeO}_2$ ) additive in the electrolyte were studied in [17].

A 20 kW power source was used for oxidation and the electrolyte was a solution of 4 g/l  $\text{Na}_2\text{SiO}_3$  and 3 g/l KOH. The oxidation time was 30 minutes and the applied current density was 0.15 and 0.3  $\text{A}/\text{cm}^2$ . The current density was found to have a direct effect on the phase composition and pore size of the oxide coatings. With increasing current densities, the concentration of rutile  $\text{TiO}_2$  was found to increase. When the concentration of the  $\text{CeO}_2$  additive was increased, the rutile concentration was found to increase further. An increase in current density also resulted in coatings with a larger pore size, increased thickness and surface roughness.

#### **c) Using an aluminate based electrolyte**

The impact of concentration of sodium aluminate ( $\text{NaAlO}_2$ ) on the properties of PEO coatings formed on pure titanium were studied in [18]. The electrolyte solution was comprised of 5 g/l  $\text{Na}_2\text{SiO}_3$ , 0.1 g/l NaOH and 3 ml/l  $\text{C}_3\text{H}_8\text{O}_3$  (glycerol). The concentration of  $\text{NaAlO}_2$  was varied from 0 to 0.4 g/l and the applied current density was 50  $\text{mA}/\text{cm}^2$ .

For  $\text{NaAlO}_2$  concentrations of 0 - 0.1 g/l, the pore size was 1  $\mu\text{m}$  or smaller with a relatively high pore density. Increasing the  $\text{NaAlO}_2$  concentration resulted in a better coating growth rate with an increase in pore size and densification of the coating. At lower  $\text{NaAlO}_2$  concentrations, the presence of a metastable  $\text{TiO}_2$  phase was observed in the coating. On increasing the concentration of  $\text{NaAlO}_2$ , this phase was found to disappear and more anatase  $\text{TiO}_2$  was observed.

### **2.3.2. Influence of current density**

The effect of current density on PEO coatings formed on titanium was studied in [19]. The power source was a pulsed DC source with a maximum output voltage of 1000 V. The electrolyte used was a solution of 16 g/l  $\text{NaAlO}_2$  and 2 g/l NaOH. The oxidation time was 40 minutes and the current density was varied from 3  $\text{A}/\text{dm}^2$  to 10  $\text{A}/\text{dm}^2$ .

The current density was found to have an effect on the phase composition of the coatings. With an increasing current density, the amount of rutile  $\text{TiO}_2$  was found to increase. At lower current densities, the amount of anatase  $\text{TiO}_2$  was more than that of rutile. The pore size and pore density were found to increase and decrease on increasing the applied current density. It was also found that samples processed at higher current densities exhibited a smoother surface morphology.

### 2.3.3. Influence of duty cycle and frequency

The effect of duty cycle and applied frequency on the growth behavior of coatings formed by PEO were discussed in [15]. The workpiece were discs of an aluminum alloy, 3 cm in diameter and 7-9 mm thick. A square waveform, pulsed DC power source was used in galvanostatic mode with a constant current density of 1.5 A/cm<sup>2</sup>. The electrolyte was a solution of 2 g/l Na<sub>2</sub>SiO<sub>3</sub> and 2 g/l KOH and the oxidation time was 30 minutes. To determine the impact of frequency, the samples were coated using applied frequencies of 50, 500, 1000 and 2000 Hz. There was no considerable difference in breakdown voltage of the samples processed at different frequencies. It was also observed that the breakdown voltage decreased with higher duty cycles. Additionally, it was observed that when constant frequencies were used, the coating growth rate increased with decreasing duty cycles.

## 2.4. Thermal stability of oxide coatings of titanium and its alloys at high temperatures

### 2.4.1. Titanium alloy (Ti6Al4V)

The anti-oxidation properties at 700 °C and thermal shock resistance at 850 °C of titania coatings formed by PEO were studied in [20]. The electrolyte was a solution of 0.3 M sodium phosphate (Na<sub>3</sub>PO<sub>4</sub>) and 6 g/l Al<sub>2</sub>O<sub>3</sub> particles. A voltage of 500 V was applied along with a frequency of 2000 Hz, a duty cycle of 60% and an oxidation time of 10 minutes. Two samples were used for testing. One which was treated with the addition of Al<sub>2</sub>O<sub>3</sub> particles in the electrolyte was termed as TMPAL and the other which was treated without addition of Al<sub>2</sub>O<sub>3</sub> particles in the electrolyte was termed as TMP. It was found that coatings for both TMP and TMPAL possessed good anti-oxidation characteristics at 700 °C. The addition of Al<sub>2</sub>O<sub>3</sub> particles helped in improving the thermal shock resistance at 850 °C due to its low coefficient of thermal expansion.

Another group of researchers have studied the high temperature oxidation resistance of PEO formed oxide coatings on Ti6Al4V [21]. The electrolyte was a solution of 4 g/l Na<sub>2</sub>CO<sub>3</sub>, 0.5 g/l NaOH and Na<sub>2</sub>SiO<sub>3</sub> in concentrations of 5, 10, 15 and 20 g/l. The process parameters were 1.2 A/dm<sup>2</sup> current density, 100 Hz applied frequency, 40% duty cycle and 25 minutes oxidation time. Of all the coated samples, it was found that the coatings formed in the 15 g/l Na<sub>2</sub>SiO<sub>3</sub> electrolyte possessed the best thermal shock resistance under experimental temperatures of 800 °C. With increasing coating thickness, the heat resistance was found to increase. At high temperatures, it was observed that the coating morphology did not change but the phase composition showed significant changes due to high temperature oxidation.

## 2.4.2. Pure titanium

The thermal stability of TiO<sub>2</sub> films formed on pure titanium was studied in [22]. The workpiece used in their research were commercially pure titanium sheets with dimensions 10 mm x 10 mm x 2 mm. The electrolyte used was pure sodium phosphate (Na<sub>3</sub>PO<sub>4</sub>) and the applied current density and voltage were 33 mA/cm<sup>2</sup> and 200 – 220 V. From XRD results, the titania coatings were found to contain anatase and rutile as the main crystalline phases. When the coated samples were annealed at 600 and 800 °C, some anatase peaks disappeared while new rutile peaks appeared, indicating that rutile is the high temperature phase of titania. With the increase in annealing temperature, the hardness of the coatings was found to increase which can be ascribed to the formation of rutile TiO<sub>2</sub>. It was also found that the thermal stability of the titania coatings remained good up to 800 °C.

## 2.5. Plasma electrolytic oxidation on porous titanium

There are few studies in which plasma electrolytic oxidation has been carried out on porous titanium [23][24]. The aim of their research was for biomedical applications. However, it was observed that the process by which the oxidation is carried out is similar to that of non-porous titanium.

Literature focusing on coating growth, formation and structure on porous titanium is rather scarce but from [23] and [24], it was noticed that the influence of electrical parameters such as voltage, current density and oxidizing time follow a similar trend as that on non-porous or bulk titanium samples.

## 2.6. Tuning the thickness and pore size of the coatings

During the PEO process, it is crucial to obtain a coating with a desired coating thickness, pore size and porosity, especially for membrane and catalyst applications. A number of factors play a role in determining these parameters such as the applied frequency, duty cycle, voltage and current density. The impact of current density on the coating structure and characteristics were studied in [25]. The workpiece was commercially pure titanium grade 2 in the form of rods. A DC unipolar pulsed source was used with an electrolyte solution containing 0.1 M KOH in water and the oxidation time was varied from 5 to 40 minutes.

For a current density of 50 A/cm<sup>2</sup> and oxidation time of 10 minutes, the thickness and pore size of the coatings were found to be 1.2 μm and 230 nm. On increasing the current density, the coating thickness and pore size was found to increase as well. However, it was observed that when the applied current density was above a certain value, more energetic and ‘violent’ discharges were observed on the sample surface. This phenomenon was found to be detrimental as it resulted in the formation of microcracks on the coating surface. Therefore, by varying the applied current density and oxidation time, the coating thickness and pore size can be tailored based on the requirement of the application.

## 2.7. Coating phases of titania formed by plasma electrolytic oxidation

One of the most abundantly available titanium alloys is Ti6Al4V and it has also been used extensively for PEO. The phase structure of the titania films formed by plasma electrolytic oxidation on Ti6Al4V workpieces were reported in [26].

Titania ( $\text{TiO}_2$ ) exists in three polymorphic phases. Polymorphism refers to the ability of a compound to exist in more than one crystal phase. The three phases of titania are anatase, brookite and rutile [26]. Out of these three phases, rutile is the most stable. It also possesses the highest micro hardness and is a major contributor to the hardness and mechanical stability of titania coatings. This is also one of the distinguishing features between PEO and anodization. The titania coatings formed by anodization are mostly amorphous rather than crystalline [27].

At low applied voltages, it was found that the coatings contained rutile and a small amount of anatase  $\text{TiO}_2$ . At a voltage of 350 V, no anatase was detected and the coating contained only rutile  $\text{TiO}_2$ . This variation of phase composition was also reported in [28]. Anatase is a low temperature crystalline phase of titania. Therefore, at higher temperatures and pressures caused by micro-arc discharge, anatase can convert to rutile and this phase transformation is expected to occur at temperatures above 500 °C.

## 2.8. Plasma electrolytic oxidation on titanium foams

Metal foams as workpieces are becoming increasingly attractive owing to their porous structure. As a result, they possess desirable physical and chemical properties such as high hardness coupled with a very low density compared to bulk metal samples. They also possess other properties such as low thermal conductivity, good permeability, high temperature and chemical resistance. In order to further improve the properties of these porous metals, surface modification techniques like PEO are used.

PEO has been used on a metallic foams such as aluminum, its various alloys and magnesium [20–24], detailing how the PEO process is responsible for enhancing the tribological and mechanical properties of the foam workpieces. Titanium foams have also been processed by PEO [34] but not as extensively as aluminum, magnesium or their alloys.

The metal foams used [34] were made of Ti6Al4V fabricated by replication and powder metallurgy. The samples used had a dimension of 40 x 40 x 20 mm<sup>3</sup>. An electrolyte solution containing 4 g/l  $\text{Na}_2\text{SiO}_3$ , 10 g/l  $\text{Na}_3\text{PO}_4$  and 20 g/l  $\text{NaAlO}_2$  was used and the oxidation time was 10 and 20 minutes. The formed PEO coatings possessed good homogeneity and was found to be present over the entire surface of the structure. The struts and pores of the foam were found to be coated homogeneously as well. Furthermore, the original structure of the foam was preserved along with the initial present



pore channels. The coatings showed the presence of a large amount of  $\alpha$ -Al<sub>2</sub>O<sub>3</sub> and a small amount of rutile TiO<sub>2</sub>.

## 2.9. Plasma electrolytic oxidation on 3D printed titanium scaffolds

Additive manufacture, commonly known as 3D printing is a relatively new technique that is being used to fabricate porous metallic structures. The advantage of this mode of fabrication is that their structural dimensions can be modified and tailored based on requirement. Coatings were formed by PEO on a 3D printed titanium sample for use in biomedical applications [35]. The author also mentions that there are currently no reports which focus on the effect of PEO coatings on the mechanical properties of 3D printed titanium scaffolds.

The 3D printed scaffold samples were made of Ti6Al4V alloy and its dimensions were approximately 7 mm in length and 10 mm in diameter. It was processed in an electrolyte solution containing 24 g/l calcium acetate and 4.2 g/l calcium glycerophosphate. A galvanostatic process was used to produce the coatings with a constant current density of 200 mA/cm<sup>2</sup>.

Four different scaffolds were used and their details are shown in figure 2-5. As the strut and pore sizes of the different samples vary, the density, porosity and the macro structure of the scaffold samples vary as well.


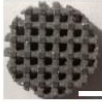
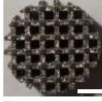
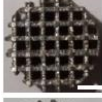
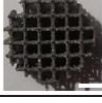
Scaffold	Unit cell shape	Strut size ( $\mu\text{m}$ )	Pore size ( $\mu\text{m}$ )	Relative density (%)	Porosity (%)	Total surface area/volume ( $\text{mm}^{-1}$ )	Macro structure (scale bar: 250 $\mu\text{m}$ )
A	Cubic 	823 $\pm$ 230	1020 $\pm$ 311	37	63	46	
B		693 $\pm$ 200	1155 $\pm$ 354	28	72	51	
C		654 $\pm$ 190	1139 $\pm$ 359	24	76	58	
D		451 $\pm$ 147	1413 $\pm$ 366	13	87	77	

Figure 2-5 Structure and dimension of the 3D printed scaffold samples [35]

The surface morphology was found to change distinctly after processing by PEO. This was observed in the form of a porous coating over the entire surface area of the sample. When the oxidation time was increased from 2 to 5 minutes, there was no evident change in the coating's macrostructure. However, micropores could be seen on the surface of the coating. An increase in oxidation time resulted in an increased deposition of electrolyte components (Ca and P) on the coating. Coatings with a thickness of 4.9  $\pm$  0.4  $\mu\text{m}$  and 9  $\pm$  2.3  $\mu\text{m}$  were produced for oxidation times of two and five minutes.

## 2.10. Plasma electrolytic oxidation on tubular samples

PEO has been extensively performed on metals with conventional geometries such as sheets, discs, cubes, etc. Data and reports for PEO performed on tubular samples are by contrast, quite scarce. A group of researchers studied the formation of PEO coatings on aluminum and steel tubes [36][37].

The principle which differentiates tubular and conventional structures in PEO is the coating of the inner wall of the tube. Since both the inner and outer walls of the tube are exposed to the electrolyte, both regions will undergo oxidation to form oxide coatings. In the case of tubes, it was found that the inner wall was coated more unevenly compared to the outer wall. This was attributed to a phenomenon called the shielding effect which arises as a result of the outer wall shielding the inner wall from the potential fields originating from the counter electrode. As a result, voltage drops are seen across the inner wall of the tube resulting in the formation of uneven and sub-optimal coatings. To circumvent this shielding effect, an extra electrode termed as the central accessory electrode, is placed through the center of the tube. A diagrammatic representation of the setup used in [36] is seen in figure 2-6. Tests were done for two sample configurations. One which used the central accessory electrode and the other which did not.

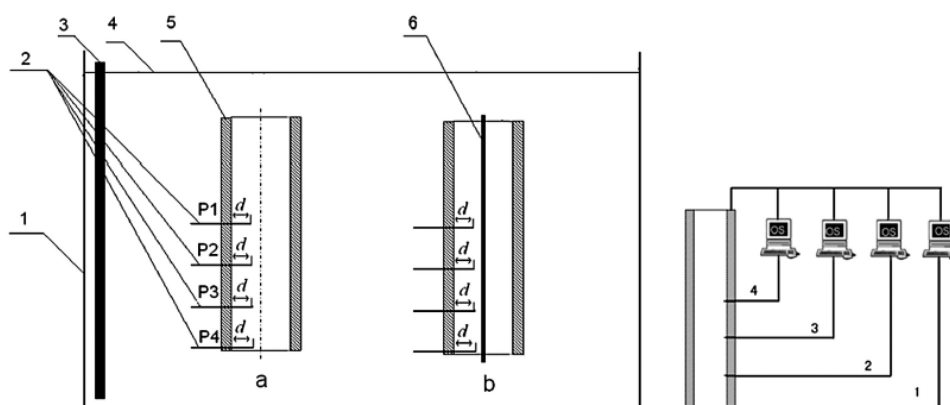


Figure 2-6 Experimental setup to coat tubular structures. (1) electrolytic bath (2) voltage probes (3) stainless steel cathode (4) surface of the electrolyte (5) tube to be coated (6) central accessory electrode [36]

Voltage probes were used to measure the voltage drop across the inner wall of the tubes. The coated tube samples were 10 mm in diameter and 100 mm in length and made of aluminum. It was found that without the central accessory electrode, the voltage drop from the bottom surface of the tube's inner wall to a distance of 5 cm from the bottom of the tube was 50 V when the applied voltage was 300 V as shown in figure 2-7. However, when the central accessory electrode was used, it was found that there was virtually no potential drop across the inner wall as seen in figure 2-8. Hence, the authors concluded that the shielding effect had been successfully overcome and uniform coatings could be produced on both walls of the tube samples.

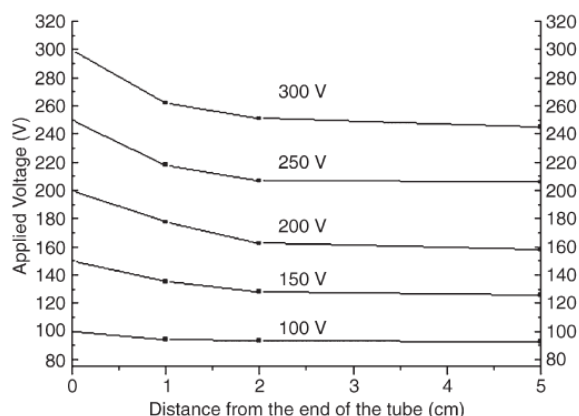


Figure 2-7 Voltage drop without using the central accessory electrode [36]

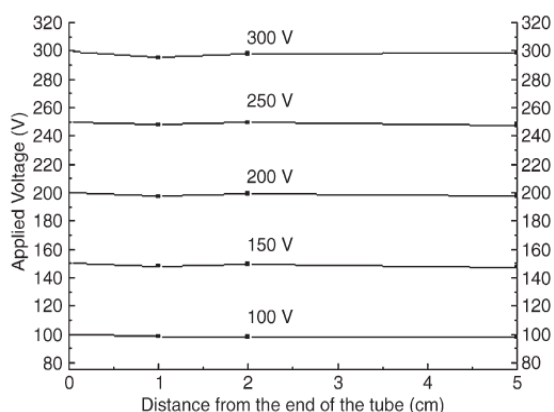


Figure 2-8 Voltage drop when using the central accessory electrode [36]

## 2.11. Plasma electrolytic oxidation on non-valve metals

Plasma electrolytic oxidation is known to be performed extensively on the so called ‘valve metals’ [38]. These valve metals refer to a certain group of metals in the periodic table which possess stable oxides and strong tendency to undergo oxidation. It is also worth noting that there are some metals which are considered to be unsuitable for PEO. These include metals such as Fe, Ni, Cu, Sn and their alloys. Interestingly, PEO has been performed on steels and is explained in section 2.12.

The tendency of a metal to undergo oxidation in an electrolytic solution is influenced by its thermodynamic properties. The most important of which is its free energy change. This refers to the potential of a metal to oxidize at ambient temperatures. For all metals except gold, the free energy change is negative, implying that oxidation would be energetically favorable in virtually all cases. However, during PEO, as plasma is created, collapses and cools, there may be other competing oxidation reactions for which the driving force of oxidation is higher. An example of which could be oxidation of molecular hydrogen to form water as the electrolytes used are usually aqueous solutions. Therefore, it can be said that if the oxidation of the metal ion is to occur, it should in principle be higher than the driving force of the oxidation of hydrogen to form water. The values of free energy of

oxide formation for some oxides are shown in figure 2-9 [38]. This hypothesis only serves as a possible explanation for why PEO can only be performed on some (valve) metals.

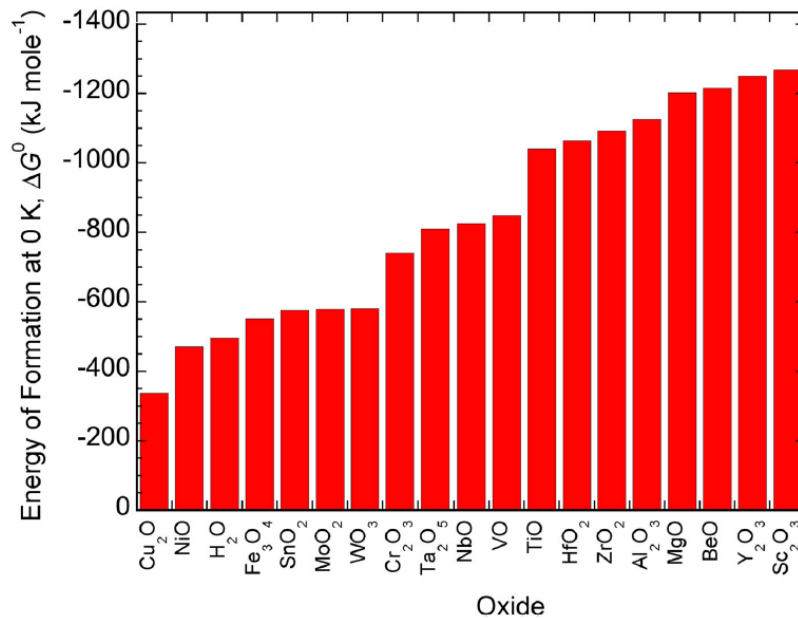


Figure 2-9 Free energy of formation for various oxides [38]

From figure 2-9, it can be seen that the oxides of copper and nickel have formation energies lower than that of water. This could be a reason for why pure copper and nickel are unsuited for PEO and is also the conclusion based on research. However, these metals can be processed by PEO by heavily alloying them with other elements that have a higher tendency to oxidize. Some examples include NiCr, Ni-Ti alloys, etc. Another method to form passivating oxide layers on these metals is to first coat them with a PEO compatible metal such as aluminum and then process the compound structure. This approach is generally used for coating those metals that are unsuitable for PEO.

## 2.12. Plasma electrolytic oxidation on steel

It is a general assumption that steels are unsuitable for coating by plasma electrolytic oxidation. This can be realized from figure 2-9, where the free energy of oxidation of iron is only slightly higher than that of hydrogen to form water. Most steels, be it carbon or alloyed steels have iron as their major constituent.

However, there are few reports of coatings formed on steels of different kinds by PEO. These include carbon steels [28–32], Ck45 steel [44] and 39NiCrMo3 steel [45]. A review of PEO coatings formed on steels in general has been performed in [46]. Some of these reports indicate that a strong, adherent coating of Fe<sub>3</sub>O<sub>4</sub> had been produced on the sample surface. However, a few of these reports also indicate that the coatings formed were largely due to deposition from the electrolyte and not by actual oxidation of the steel substrate. In most of the reports of PEO coating on steels, Al<sub>2</sub>O<sub>3</sub> was used as an

additive in the electrolyte. This was to add mechanical strength to the formed iron oxide layer and also to stabilize it and improve the its corrosion resistance.

### 3. Materials and methods

#### 3.1. Experimental setup and samples processed

The experimental setup used for PEO is shown in figure 3-1. The electrolytic bath (D) is jacketed and its inlet and outlet were connected to a *LAUDA Ecoline RE 104 thermostat* (A) which functions as the cooling system. In order to ensure uniform mixing and agitation of the electrolyte during the process, a magnetic stirrer (B) was used along with a suitably sized magnetic pellet. The electrical connections to the two terminals of the power supply were established by a banana plug - crocodile clip connection for both the counter electrode (C) and the workpiece being coated (E). The counter electrode (C) was a sheet of stainless steel with dimensions 5 cm x 3 cm and was sourced from the Equipment and Prototype Centre (EPC), Eindhoven University of Technology.

Prior to starting the experiments, the coolant flowing through the tubes were set to a temperature of 9 °C to obtain a larger amount of heat exchange between the electrolyte and coolant, thereby helping in reducing the maximum temperature attained during an experimental run. The electrolyte temperatures were measured prior to beginning the experiment and after the experiment using a *Precision multi-thermometer*. The power source used for experimentation was a *SPM SP300VAC*, AC power source rented from Caltest instruments GmbH, Germany. It had a maximum power output of 2 kW and a maximum output voltage of 300 V<sub>AC</sub>. For the experiments, a maximum current limit of 6.5 A was set. All the experiments were performed under Potentiostatic (constant voltage) mode. Potentiostatic refers of a mode of operation where a constant voltage is set at the beginning of the experiment and during the process, the output current and power varies based on the set input voltage and the system's electrical parameters.

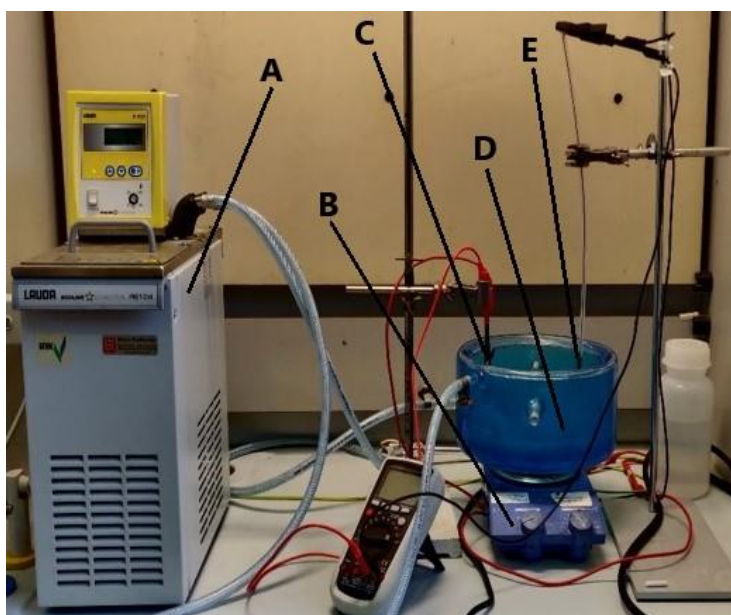


Figure 3-1 Experimental setup used for PEO where; A) cooler B) Magnetic stirrer C) counter electrode D) electrolytic bath E) workpiece being coated

Samples with different geometries that were processed by PEO are detailed below. The method by which the samples were connected to the power source was dependant on their geometry.

### **Material selection**

Titanium was chosen as the primary base material for the catalyst and membrane applications due to its high hardness, mechanical strength and melting point (1668 °C). As the working temperatures of the catalyst and membrane application could reach 800 °C, it is important that the base metal can withstand those temperatures. Metals such as Al or Mg which are also suitable for PEO have melting points of 663 and 650 °C and are therefore unsuitable for this application. Titanium can also be sourced in a number of different forms known as ‘grades’ based on their workability and hardness which is an added advantage as it adds flexibility to the selection of the titanium sample.

#### **a) Titanium discs**

Disc samples with diameters 1 and 1.5 cm were fabricated from a 15 cm x 15 cm titanium plate with a thickness of 4mm, sourced from Salomon’s Metalen B.V (Groningen, the Netherlands). The plate was made of commercially pure titanium, grade 2. In order to connect the disc samples to one of the terminals of the power source, a 3 mm diameter threaded hole was drilled into its lateral surface. To ensure proper electrical contact between the power source and the workpiece, a nylon screw with a diameter of 3 mm was screwed into the threaded hole of the titanium disc. Electrical contact was made by means of a 0.5 mm copper wire which was passed through a hole made through the centre of the nylon screw. At the tail end of the screw, the copper wire was fashioned into a bulb which formed the electrical point of contact with the titanium disc samples. A picture of this connection is shown in figure 3-2. The other end of the copper wire is connected to one of the terminals of the power source by a crocodile clip.



*Figure 3-2 Electrical connection for the 1 and 1.5 cm diameter titanium disc samples*



### b) Titanium wire and wire bundles

A spool of titanium wire was sourced from Nanjing Youtian Metal Technology Co., Ltd, China. The thickness of the wire was 300  $\mu\text{m}$ . For the experiments, multiple wires (3 at a time) and wire bundles (20 wires) were processed by PEO. The length of the wires used in the experiments were approximately 4 cm and the connections to the power source were made by direct contact with a crocodile clip. The connections for both the multiple (three) titanium wire and titanium wire bundle samples are shown in figure 3-3. For the three titanium wire samples, the contact is directly made via the crocodile clip and the wires are immersed into the electrolyte with some portion of the wire remaining above the surface of the electrolyte.

The wire bundle samples comprised of 20 wire wires of equal length (approximately 4 cm), which are wound with titanium or zirconium wire. The wires used for winding are then connected to the power source by means of a crocodile clip. In this configuration, the entire bundle could be immersed in the electrolyte and the winding wires act as the current carrier to the immersed bundle samples.

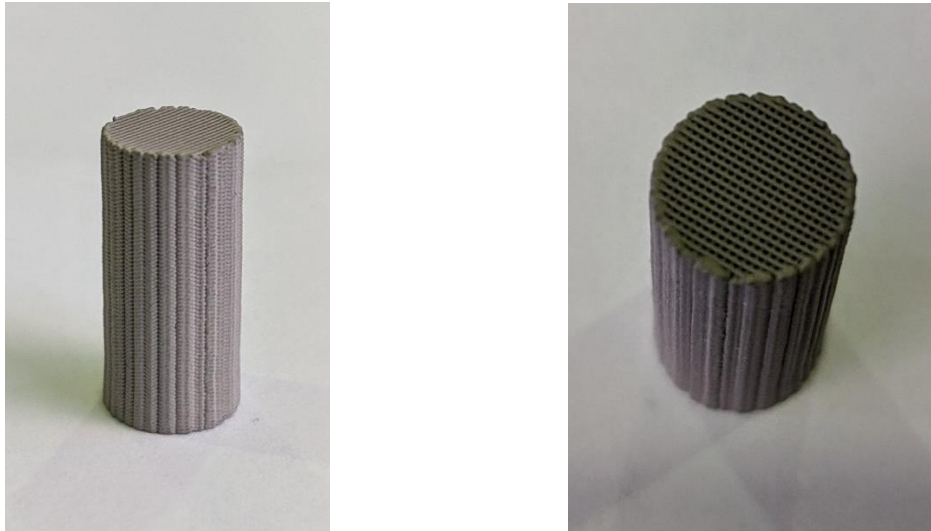


*Figure 3-3 Connections for left) three titanium wires; right) titanium wire bundle*

### c) 3D printed titanium scaffold

Titanium scaffolds fabricated by 3D printing were sourced from VITO in Belgium. Those used in experimentation were 2 cm in length and were relatively porous in nature owing to their strut like and hollow nature as seen in figure 3-4.





*Figure 3-4 Visualisation of the 3D printed titanium scaffold left) front view; right) top view*

These samples were processed in two different ways. The first was by direct contact of the workpiece with a crocodile clip. This configuration meant that only a part of the workpiece could be immersed in the electrolyte during the coating process. The second method was by winding a scaffold with titanium wire similar to the titanium wire bundle samples, thereby ensuring that the entire wound scaffold sample was immersed in the electrolyte during the coating process. This type of connection can be seen in figure 3-5, where the winding wire acts as the electrical conductor from the power source to the workpiece.



*Figure 3-5 Wound 3D printed titanium scaffold sample*

#### **d) Porous titanium tubes**

Porous titanium tubes were sourced from Stanford Advanced Materials in the United States. Their dimensions and properties are mentioned in table 4 and their picture is shown in figure 3-6.

Table 3-1 Details of the porous titanium tubes

Material	Length (cm)	Outer diameter (mm)	Wall thickness (mm)	Purity	Filter rating ( $\mu\text{m}$ )
Commercially pure Titanium	10	13	2	Min. 99.5% Ti.	0.45



Figure 3-6 Porous titanium tube

As the PEO process is influenced by the surface area of the sample, the tubes were cut into 1 cm long pieces and these pieces were used as samples for experimentation. The size and geometry of the tube samples made it mechanically difficult to establish a direct electrical connection through a crocodile clip. Therefore, they were wound with titanium wire and immersed into the electrolyte for processing by PEO as seen in figure 3-7.



Figure 3-7 Connection for the 1 cm long porous titanium tube sample

Similar to the wire bundle and wound scaffold electrical connections, the titanium wire used for winding acts as the electrical conductor from the power source to the workpiece being coated.

#### e) Zirconium wires

A spool of Zirconium wire was sourced from Nanjing Youtian Metal Technology Co., Ltd, China. The wire had a thickness of 250  $\mu\text{m}$ . Similar to the processing of the titanium wire samples, the zirconium wire samples were processed as multiple wires (3-4) and bundled (20) wire samples with a length of approximately 4 cm. The electrical connection to the power source was the same as that of the titanium wire samples which was by means of a crocodile clip.

### 3.2. Variation of process parameters

The PEO process is influenced by the applied electrical and process parameters. During the course of experimentation, the applied voltage, frequency and electrolyte type and concentration were varied as mentioned below.

- a) Voltage – Varied between 200 and 260 V depending on the surface area of the sample
- b) Frequency – Two values of frequency were applied, which were 50 and 200 Hz

In addition to voltage and frequency, the electrolyte type and electrolyte concentration were also varied as shown in table 3-2.

Table 3-2 Electrolyte details

Type of electrolyte							
Sodium metasilicate ( $\text{Na}_2\text{SiO}_3$ )				Sodium aluminate ( $\text{NaAlO}_2$ )			
Classification	Composition			Classification	Composition		
	$\text{Na}_2\text{SiO}_3$ (g/l)	$\text{Na}_2\text{SiO}_3$ (M)	KOH (g/l)		$\text{NaAlO}_2$ (g/l)	$\text{NaAlO}_2$ (M)	KOH (g/l)
Electrolyte 1 (E1)	6.103	0.05	2	Electrolyte 1 (E1)	8.197	0.1	2
Electrolyte 2 (E2)	10	0.082	1	Electrolyte 2 (E2)	10	0.122	2
Electrolyte 3 (E3)	12.206	0.1	0.5	Electrolyte 3 (E3)	12.295	0.15	2

Sodium metasilicate was laboratory grade and sourced from Alfa Aesar. Sodium aluminate was also laboratory grade and sourced from Sigma Aldrich. The impact of electrolyte concentration on the coating process was studied by using three different concentrations which were classified as E1, E2 and E3 for both electrolyte types and were chosen on a basis of increasing concentration and conductivity.

### 3.3. Material characterization

#### 3.3.1. Surface morphology

To determine the degree of homogeneity of the coatings, Scanning electron microscopy (SEM) was used. The characterization was performed using the Phenom ProX electron microscope, Eindhoven

University of Technology under 15 kV mapping and with a resolution of 64 x 64 pixels. To determine the extent of coatings formed on the processed samples, multiple regions of the samples were analyzed.

### **3.3.2. Element identification and phase composition**

In order to determine elemental composition of a certain region of the coated samples, the regions of the samples characterized by SEM, were also characterized by energy-dispersive X-ray spectrometry (EDX) using the element identification feature present on the Phenom ProX electron microscope, Eindhoven University of Technology, the Netherlands. A number of different regions on the coated surface were characterized by EDX in order to correlate the results obtained from SEM. EDX was done using the back scattering detector (BSD) of the Phenom ProX. This detector was used to obtain a better visualization of the coating as the emissions originate from deeper regions of the coated sample.

X-ray diffraction (XRD) was performed at Technische Universität Berlin with the help of Dr. ing. Oliver Görke, to determine the phase composition of the coatings.

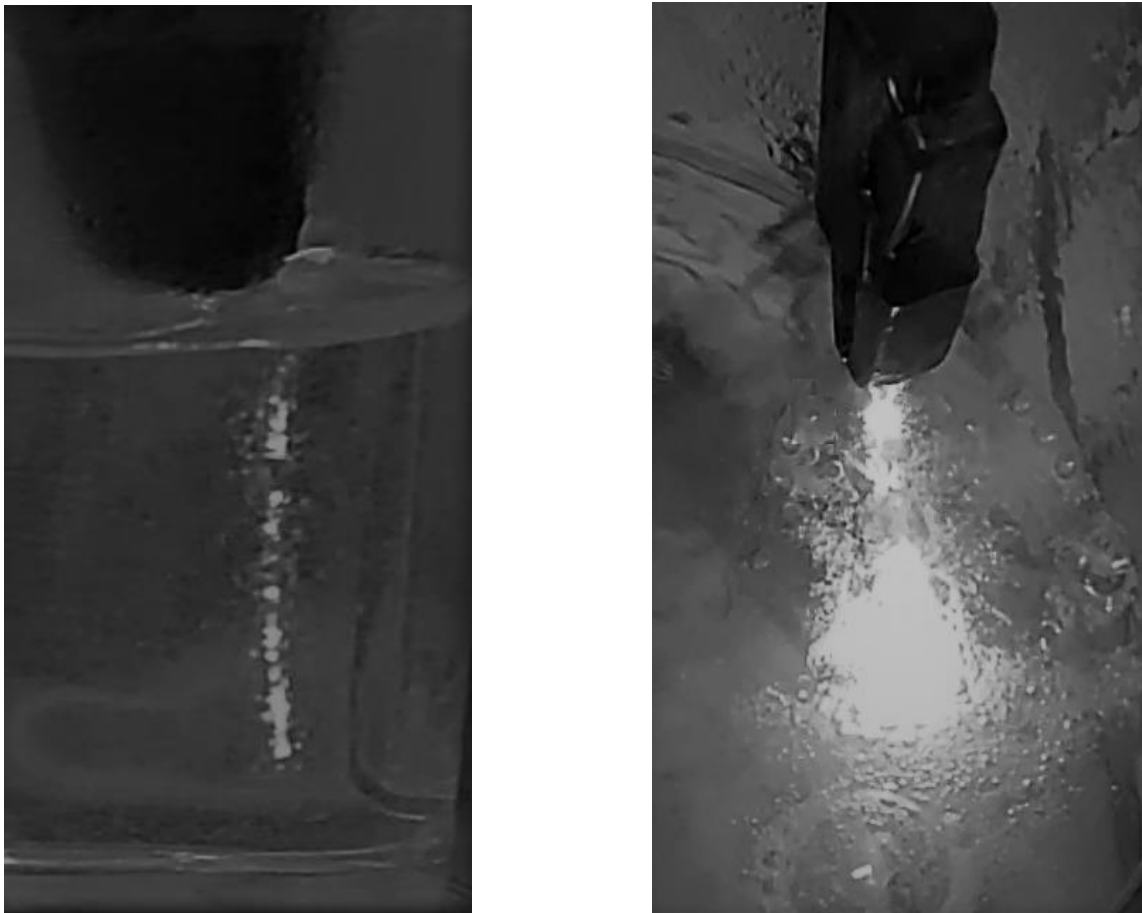
### **3.4. Current-time data**

The impact of the electrical and process parameters on the output current was studied by observing the change in current during an experimental run and plotting its variation against time to obtain a current-time graph. It was not possible to use real time data acquisition software during the course of this project. Therefore, the current-time variation was noted manually for a time interval of ten seconds and the value of current was taken from the display of the power supply unit.

## 4. Results and discussion

### 4.1. Plasma discharge phenomena and equivalent circuit diagrams

Plasma electrolytic oxidation is characterized by spark or plasma discharge on the surface of the workpiece owing to the relatively high voltages applied. Based on the applied process parameters (Section 4.2), after a certain duration of time, intense spark discharge was observed on the surface of the samples being processed. This was especially evident on the wire samples, where the distribution of the sparks was observed to be over the entire area of the immersed sample as seen in figure 4-1.



*Figure 4-1 Spark discharge observed on left) single titanium wire; right) three titanium wire sample*

The single titanium wire sample was processed at the beginning of experimentation on wire samples to study the discharge behaviour of a wire sample in the experimental setup. Once spark discharge was observed on the single wire samples, focus was given to multiple wires and wire bundle samples. Interestingly, it was also observed that the discharge phenomena was not continuous till termination of the process. Rather, there were brief intervals of time which varied from a fraction of a second to almost two seconds where the plasma discharge ceased to occur as seen in figure 4-2.

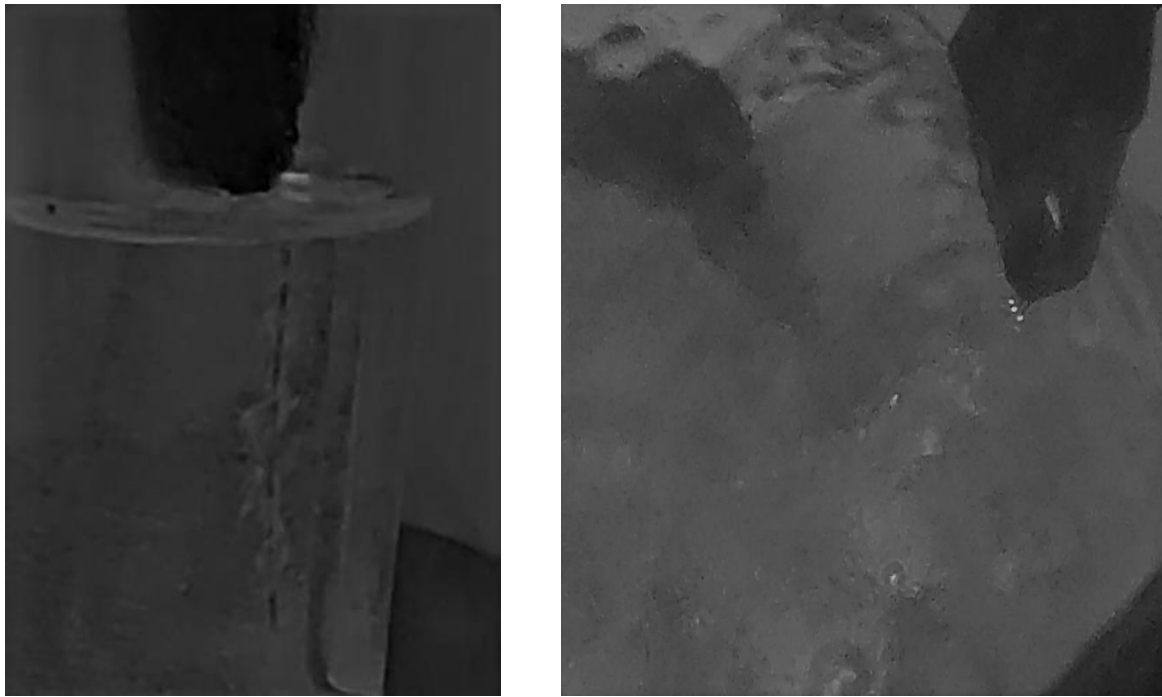


Figure 4-2 Seizing of spark discharge on the titanium wire samples

The seizing and presence of plasma discharge has a significant impact on the overall resistance of the system which can be explained by an equivalent circuit diagram (EEC) [47] of the electrical system.

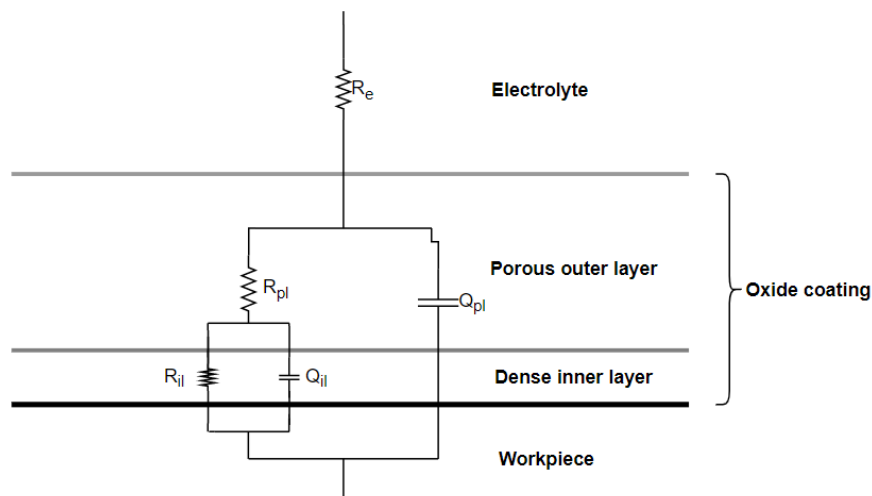


Figure 4-3 Equivalent circuit diagram representing the electrical system

Figure 4-3 shows an EEC for a system where a bi-layered coating is produced on the workpiece. The resistance components in the system are  $R_e$ ,  $R_{pl}$  and  $R_{il}$  which are those of the electrolyte, outer porous layer and the dense inner layer which contacts the surface of the workpiece. Since an Alternating current is applied in the process, capacitances of the outer and inner layer of the coating ( $Q_{pl}$  and  $Q_{il}$ ) are shown in EEC. However, the main focus is on the impact of the plasma discharge on the resistance of the system and hence, the capacitive component of the EEC is not discussed. Analysis of the EEC can also be correlated to the current-time trend (section 4.2) of samples being processed.

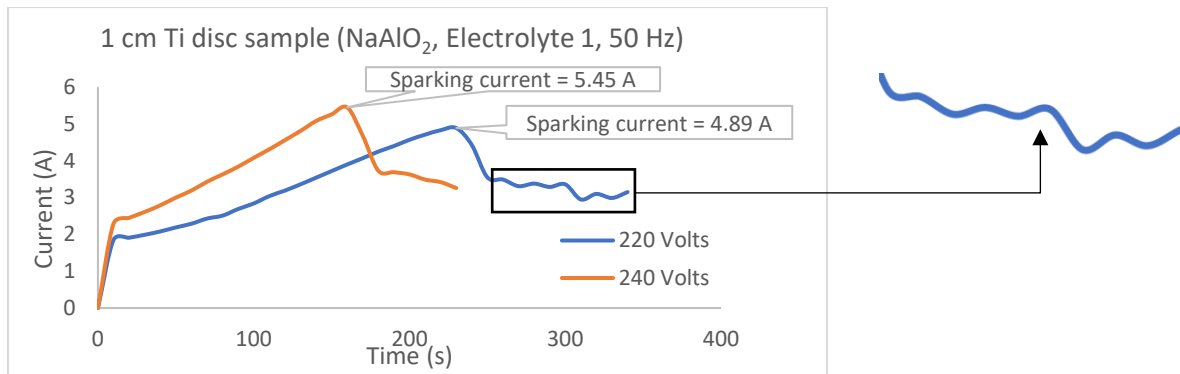


Figure 4-4 Current time graph for a 1 cm diameter titanium disc sample processed with the aluminate based electrolyte (E1) at 50 Hz

An example is explained using figure 4-4 as a reference. When the current reaches the value equal to the sparking current, it enters the intense sparking regime. It is observed from the graph that the current drops almost immediately after the onset of sparking. This could be attributed to the sudden increase in resistance around the workpiece ( $R_{ii}$  and  $R_{pl}$  from the EEC) due to the gas bubble generation and plasma discharge at the vicinity of the sample's surface. Furthermore, it is seen that after some amount of time in the sparking regime, there are irregularities in the current-time trend as seen in the highlighted portion of the graph. By visual observation of the plasma discharge and value of current, it was seen that there was a rise in current whenever the sparking seized on the surface of the sample. As soon as the sparking resumed, the current was found to drop again, resulting in the crests and troughs that can be seen in the magnified region of figure 4-4. This trend was observed for all the samples that displayed plasma discharge.

A possible method to confirm this observation would be by time-correlated observations using data acquisition software and high-speed cameras to correlate the presence of discharge phenomena with the change in value of current.

## 4.2. Current-time data

This section is divided based on the type of the samples that were processed. The current-time data for the different sample types were studied for the variation of voltage, frequency and electrolyte concentration and type. In the current-time graphs,  $t_m$  and  $A_m$  represent the process time at which sparking occurred (s) and the corresponding value of current in Amperes (A).

### a) 1 cm diameter titanium disc samples

The effect of electrolyte composition for the silicate based electrolyte can be seen in figure 4-5. A comparison is made for samples treated at 230 V, 200 Hz and 260 V, 200 Hz. This provides an insight not only into the impact of electrolyte composition but also the effect of voltage on the current generated in the system.

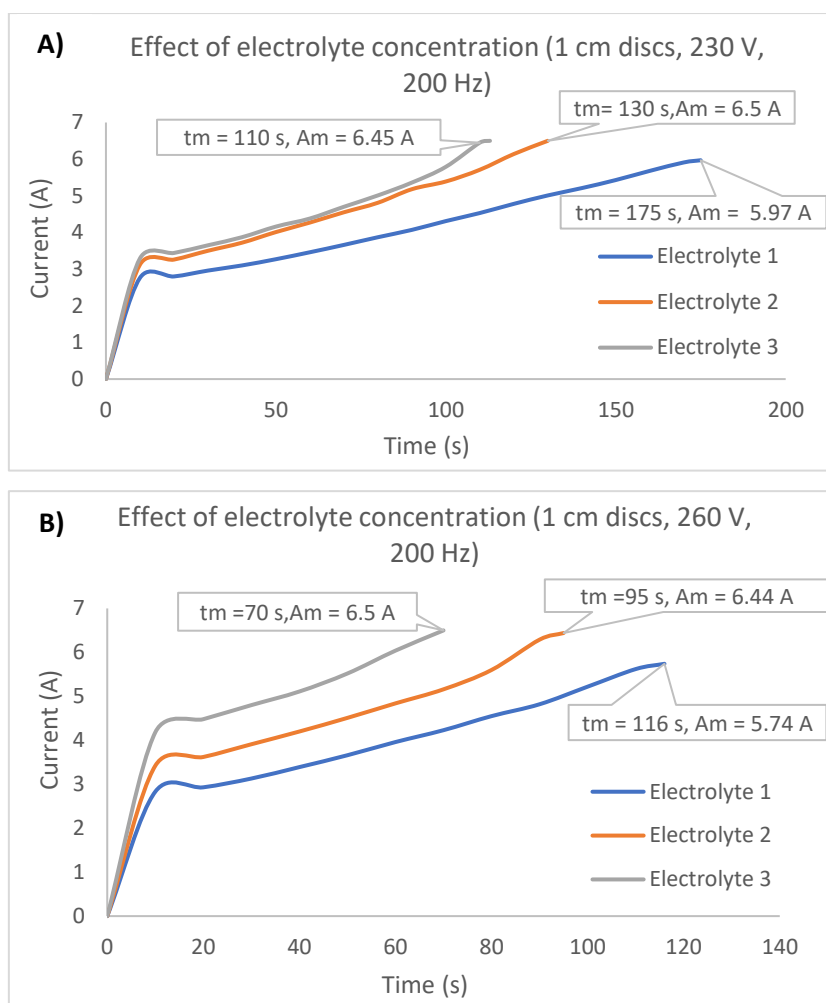


Figure 4-5 Effect of electrolyte composition for disc samples processed in the silicate based electrolyte

To control the maximum current produced in the system, a current limit of 6.5 A was inputted into the power source prior to experimentation. With this in place, when the current reached the maximum value, the process would switch from a constant voltage to a constant current (galvanostatic) process. The maximum current and the time at which the maximum current is attained is represented in the current time graphs as  $t_m$  (s) and  $I_m$  (A) respectively. Figure 4-5 gives an insight into the impact of not only the electrolyte concentration but also the applied voltage as the frequency for both A) and B) is the same (200 Hz). It can be seen that as the voltage and electrolyte concentrations increase,  $t_m$  decreases which implies that the increase in current is more rapid and hence the maximum current ( $I_m$ ) is attained at an earlier process time ( $t_m$ ).

The sample processed at 230 V and 260 V in electrolyte 1 showed plasma discharge phenomenon. Therefore, its  $I_m$  value is less than 6.5 A. For the disc samples, the process was terminated when intense sparking began. This was because, owing to their geometry and size of the sparks generated, the discharge was rather violent.



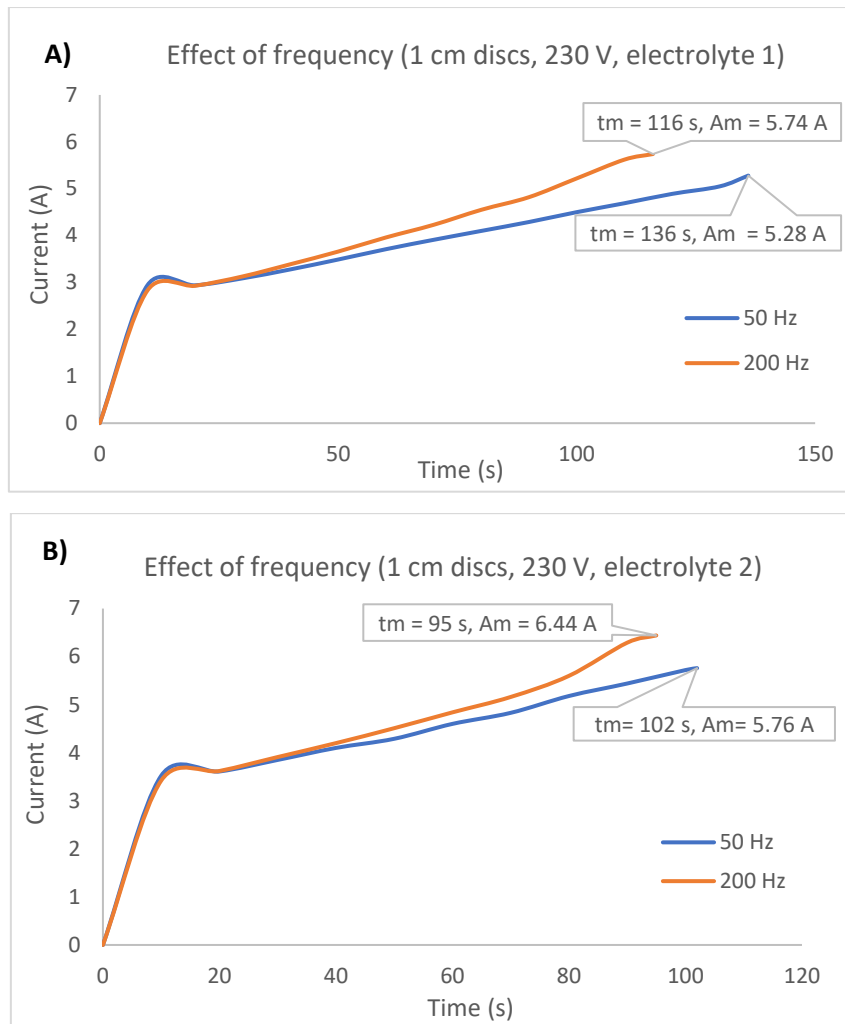


Figure 4-6 Effect of frequency A) 50 Hz; B) 200 Hz for 1 cm disc samples in the silicate based electrolyte

The effect of frequency can be realized from A) and B) of figure 4-6. The initial rise in current is the same for both frequencies. However, the rate of increase of current and maximum current reached is more for the 200 Hz samples. This could be attributed to the fact that higher frequencies produced more frequent but less energetic electrical discharges.

The impact of voltage can be seen in figure 4-7. With an increasing voltage, larger currents are generated and expectedly, the rate of increase of current is higher. Therefore, for disc samples with a high surface area ( $2.847 \text{ cm}^2$  for 1 cm discs), the process is limited by the maximum output current of the power source used for experimentation.

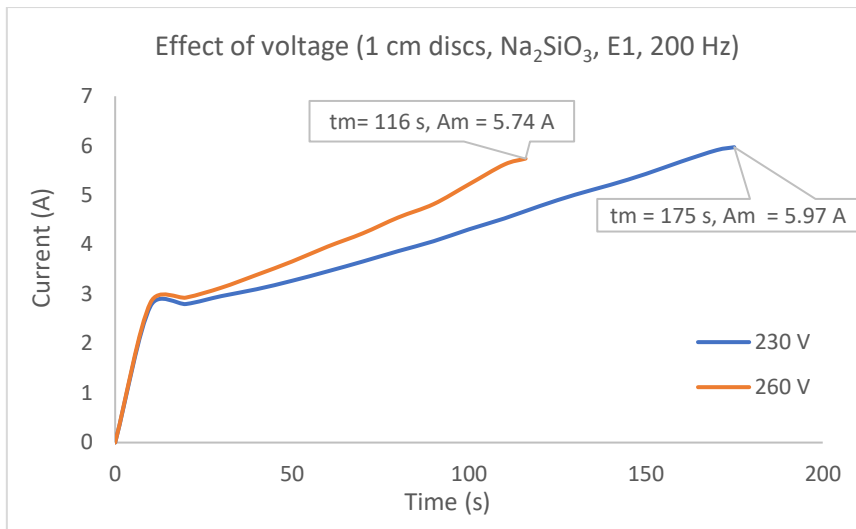


Figure 4-7 Effect of voltage for disc samples in the silicate based electrolyte

Toward the later part of experimentation on the disc samples, tests were done using the aluminate based electrolyte. From the current time data in figure 4-8, it was observed that aluminate based electrolytes are less conductive than their silicate based counterpart. As a result, it was possible to apply higher voltages without having the current reach its maximum value. The effect of voltage however is the same as that of the silicate electrolyte and intense sparking was observed for both the 220 V and 240 V samples. Even though the discharge was rather violent, the process was allowed to run for around a minute before being terminated.

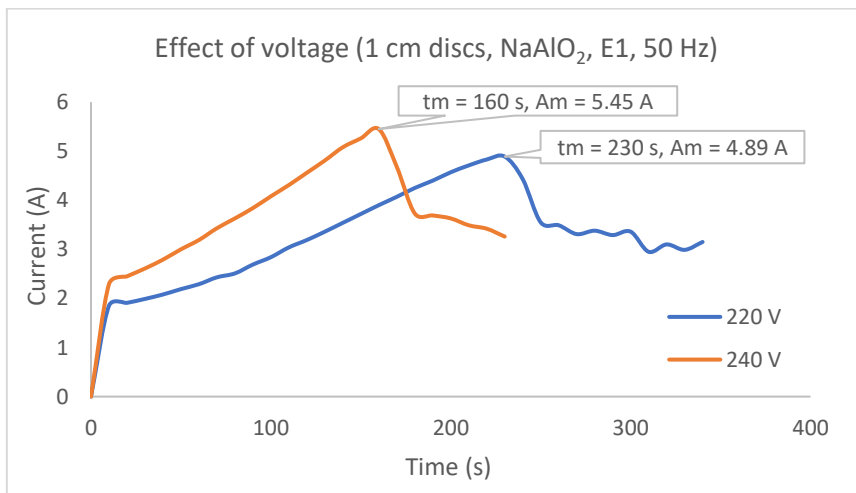


Figure 4-8 Effect of voltage for disc samples in the aluminate based electrolyte

### b) 3D printed titanium scaffolds

The current time data for the 3D printed scaffold samples processed by partial immersion in the silicate based electrolyte and direct contact with the crocodile clip is shown in figure 4-9. Since only a portion of the sample was immersed, the surface area of the sample in contact with the electrolyte was small, resulting in smaller currents being produced. Intense spark discharge was observed on all the 3D printed samples. The sparking current Am was found to increase with increasing voltage and

electrolyte concentration. The sample processed at 220 V, 50 Hz and in electrolyte 1 had a sparking current of 5.22 A which occurred at an oxidation time of 160 s. The sparking current and time for the other two samples were largely similar with an  $A_m$  of around 6.5 A and  $t_m$  of 110 s. Interestingly, it can be inferred that the effect of increased voltage (220 V to 240 V) has a similar impact as the increase in electrolyte concentration (E1 to E2).

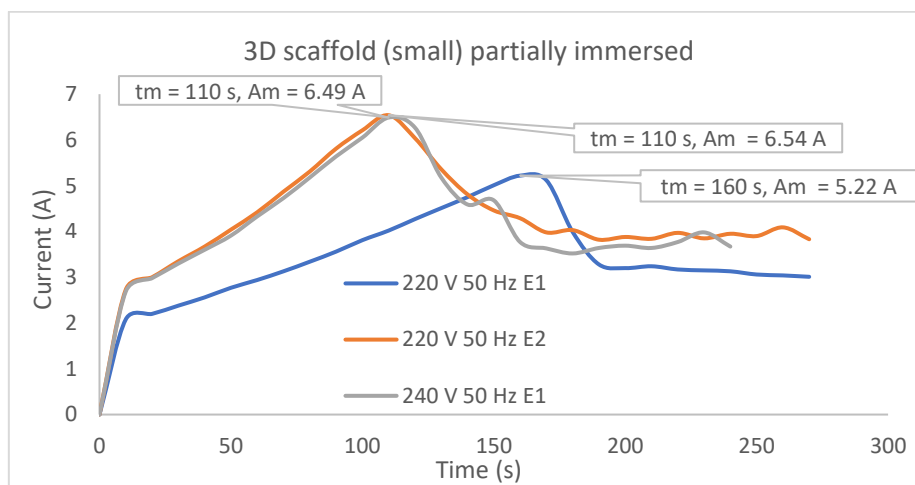


Figure 4-9 Current time data for partially immersed 3D printed scaffold samples

The 3D printed samples were also processed by winding them with a titanium wire and immersing them in the aluminate based electrolyte. The current time data for these samples is shown in figure 4-10. These samples were completely immersed in the electrolyte solution during their processing. The blue trend line in figure 4-10 is for a sample that was treated at an initial voltage of 210 V and then ramped up to 220 V during the process, after the onset of intense sparking. It was observed that the current reached the maximum value of 6.5 A for all the samples. As the current reached the maximum value, the voltage began to drop to compensate for the reducing resistance of the system due to the electrolyte temperature. As the 220 V, 210 and 210-220 V samples reached the  $A_m$  value earlier, the voltage drop occurred for longer until the plasma discharge began. This is undesirable as the applied process is Potentiostatic. Therefore, a current lower than 6.5 A is favoured in order to prevent dropping of the voltage.

The point at which the trendlines showed a sudden drop in current represent the sparking time and current. The 220 V and 210-220 V samples had a similar sparking time of 200 s while the 210 and 200 V had a similar sparking time of 230 s. Based on these results, it can be concluded that for samples with larger surface areas, lower voltages and more dilute electrolytes should be used to avoid voltage drops and the current reaching the maximum value.

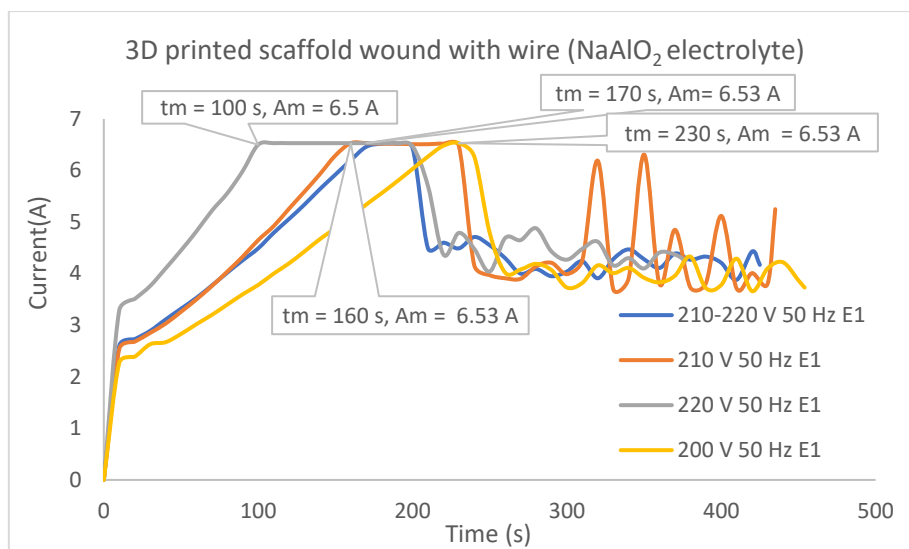


Figure 4-10 Current time data for 3D scaffold samples wound with titanium wire and processed in the aluminate based electrolyte

### c) Titanium wire and wire bundle samples

A significant amount of experimentation was done on wire samples due to their relatively lower surface area and quantity of material available. All the wire samples processed had a length of approximately 4 cm plus or minus a few millimeters as they were cut manually. Figure 4-11 shows the current time data for samples comprised of three titanium wires (3TW) based on variation of electrolyte concentration, frequency and voltage. The data is for the tests conducted in the silicate based electrolyte. All samples showed plasma discharge phenomena characterized by the steep drop in current. The sparking current ( $A_m$ ) was found to be almost similar for the samples processed at increasing electrolyte concentrations and was found to increase slightly with increasing voltages. The sparking time ( $t_m$ ) was found to decrease with both increase in electrolyte concentration and applied voltage. The impact of frequency was more evident for the wire samples processed at 220 V and 200 Hz, where it reached the maximum current value of 6.5 A.

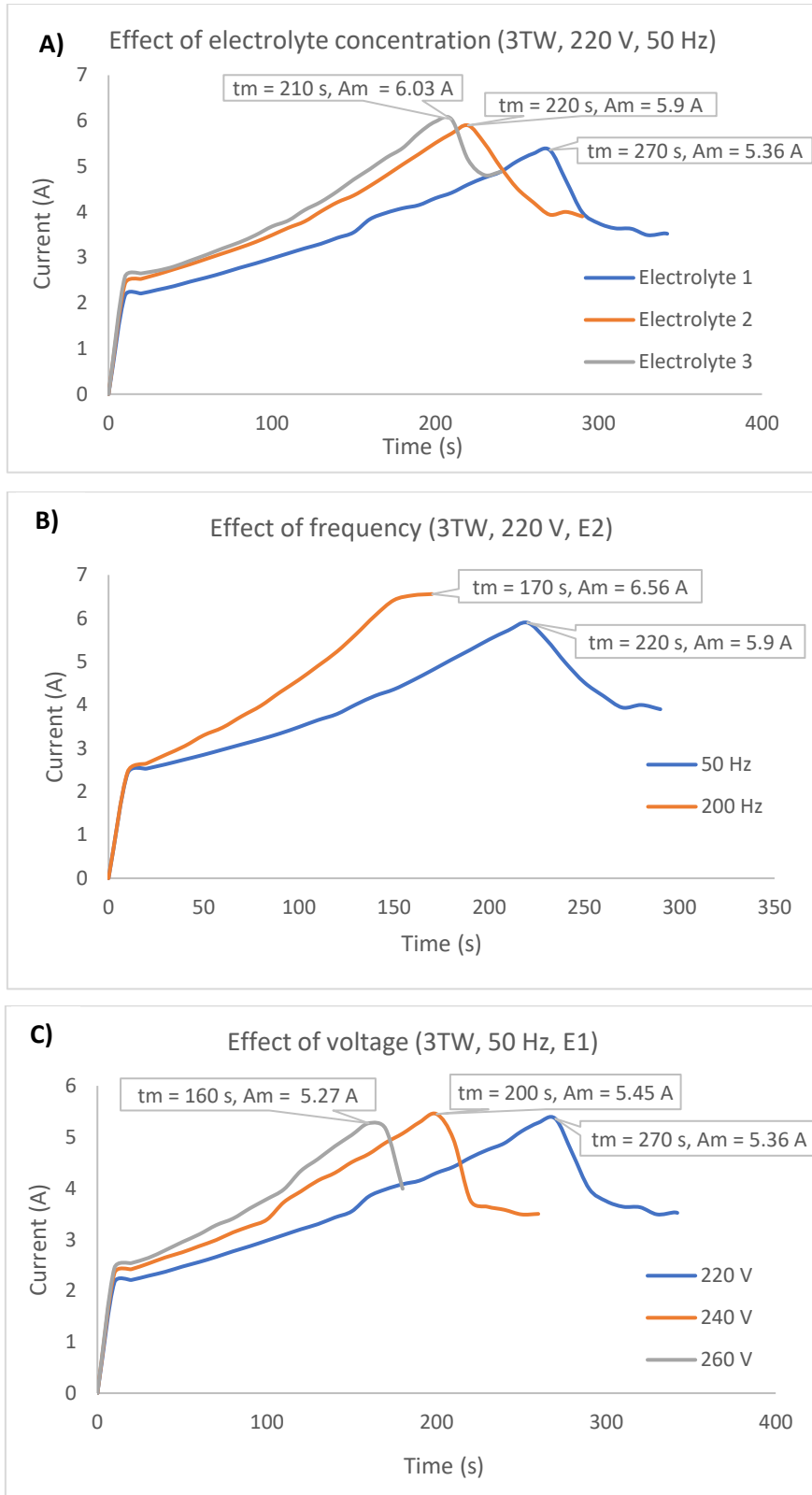


Figure 4-11 Current-time graphs for titanium wire samples for the variation of A) electrolyte concentration; B) frequency; C) voltage in the silicate based electrolyte

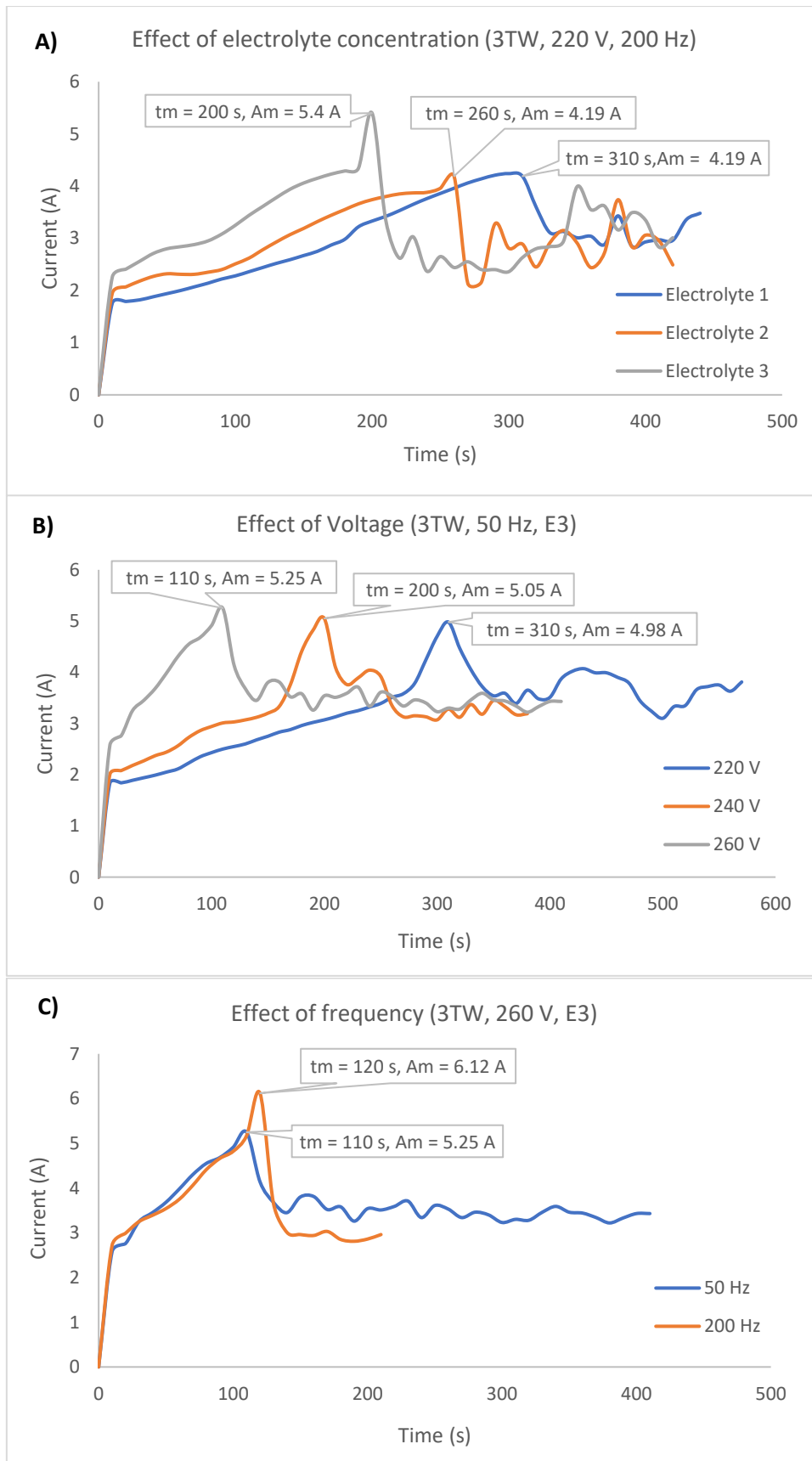


Figure 4-12 Current-time graphs for titanium wire samples for the variation of A) electrolyte concentration; B) voltage; C) frequency in the aluminate based electrolyte

Current time data for the variation of the process parameters using the aluminate based electrolyte are shown in figure 4-12. The trends were similar to those of the silicate based electrolyte but it can be seen that the currents produced are generally lower due to the aluminate electrolyte being less conductive than its silicate counterpart. In addition, the phenomena of plasma discharge stopping and resuming were observed to be more significant for the aluminate electrolyte as can be seen the variations of the trendlines of A) and B) of figure 4-12 after the onset of intense sparking. The larger crests and troughs present for the aluminate electrolyte indicate that the seizure of spark discharge occurs for a longer periods of time compared to the silicate based electrolyte.

A titanium wire bundle sample was processed in the aluminate electrolyte and its current time graph is shown in figure 4-13. Due to the larger surface area of the bundle samples as compared to the three wire samples, the sparking current was found to be higher at 5.96 A for the most dilute electrolyte (E1) at the lowest applied voltage of 220 V. Spark discharge was observed at 260 s of oxidation time and the variation of current after the onset of intense sparking was observed to be less than that of the three titanium wire samples processed in the aluminate electrolyte.

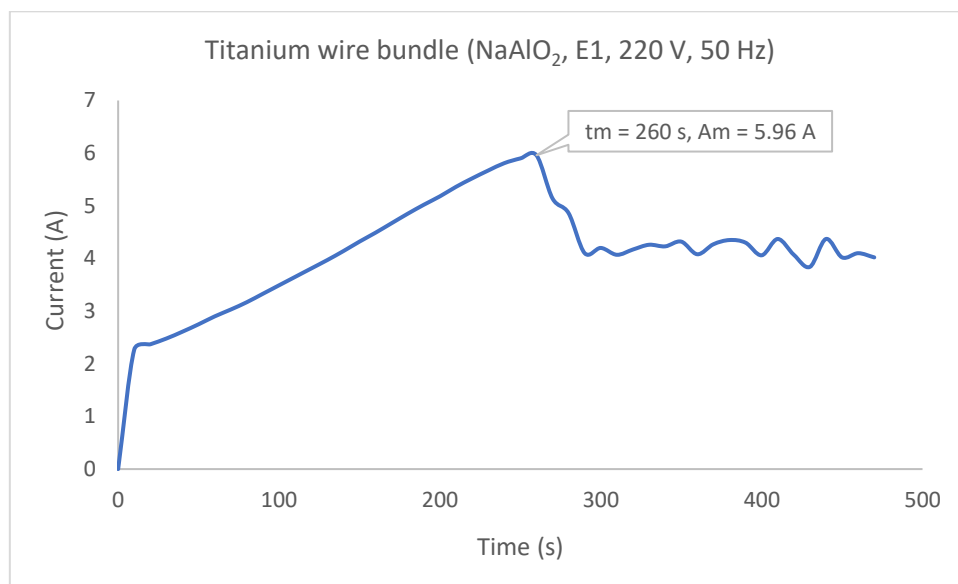


Figure 4-13 Current time data for a titanium wire bundle sample

#### d) Zirconium wire samples and wire bundles

Processing of zirconium wire samples containing 3-4 wires were done using the aluminate based electrolyte owing to its lower conductivity compared to the silicate based electrolyte. This was done with the knowledge that zirconium is more passive to oxidation than titanium and this was also observed during experimentation. This can be seen in the  $t_m$  values in figure 4-14 A) and B). Sparking for the Zr wire sample treated at 220 V, 50 Hz and E2 (figure 4-14 B) showed mild discharge after 470 s of oxidation. From figure 4-14 A), the 220 V sample does not show intense sparking even after 500 s of oxidation, whereas the 240 and 260 V samples begin sparking after 250 and 330 s of oxidation time.

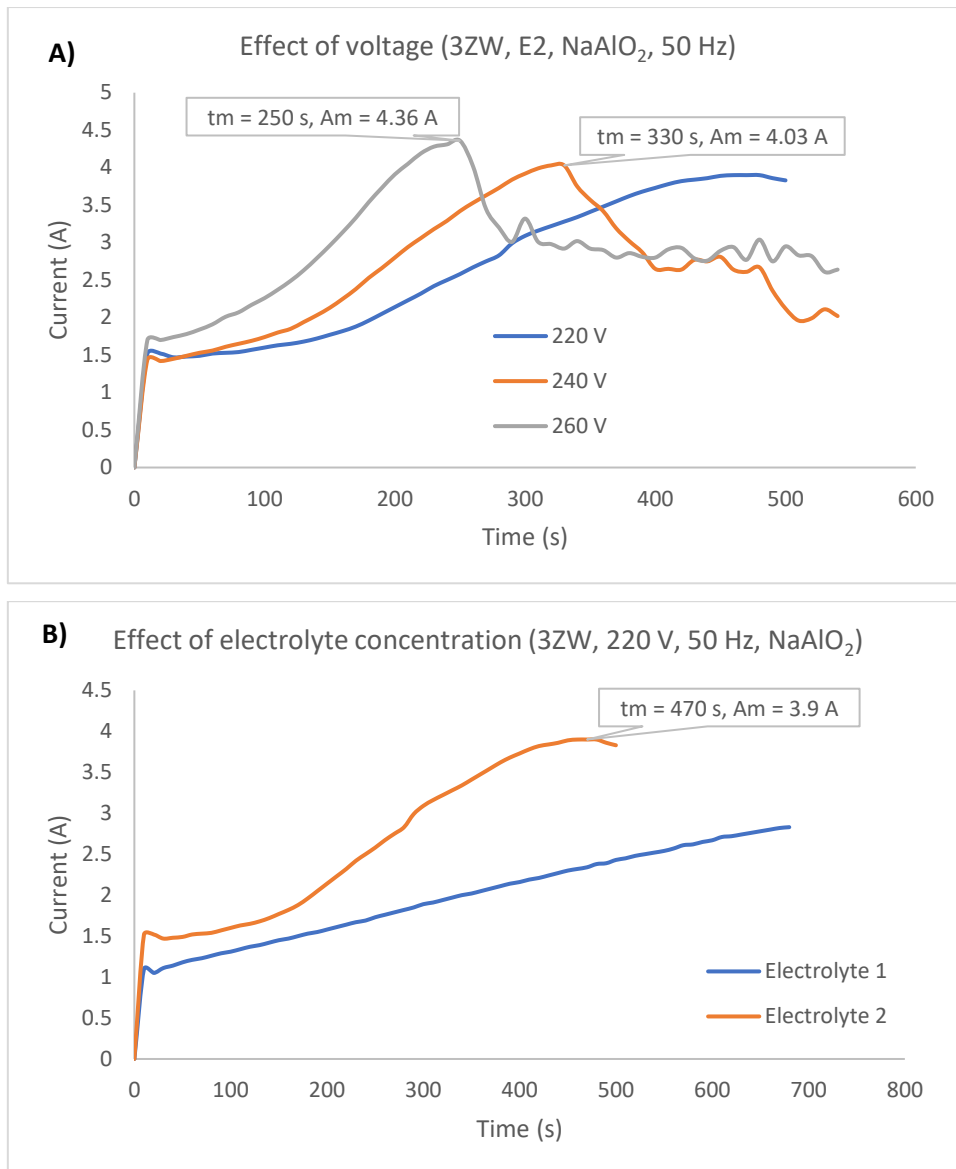


Figure 4-14 Current time data for Zr wire samples containing three wires in the aluminate based electrolyte, for the effect on A) voltage; B) electrolyte concentration

The current time data for a zirconium wire bundle sample processed in the aluminate electrolyte is shown in figure 4-15. The initial applied voltage was 200 V. It was observed that the increase in current was relatively mild and hence voltage ramps of 20 V were applied at process times of 390 and 540 s, denoted by *t ramp 1* and *t ramp 2*. On application of the voltage ramp, the current immediately showed a sharp rise in value. However, the increase soon stabilised and showed a gradual rise in value similar to the current rise prior to the ramp. On application of the second ramp, the current rose initially but then reached a value where mild discharges were produced on the surface of the sample. This was characterised by a slight decrease in the current value in the 240 V region. This trend was observed for a few more minutes before terminating the process.



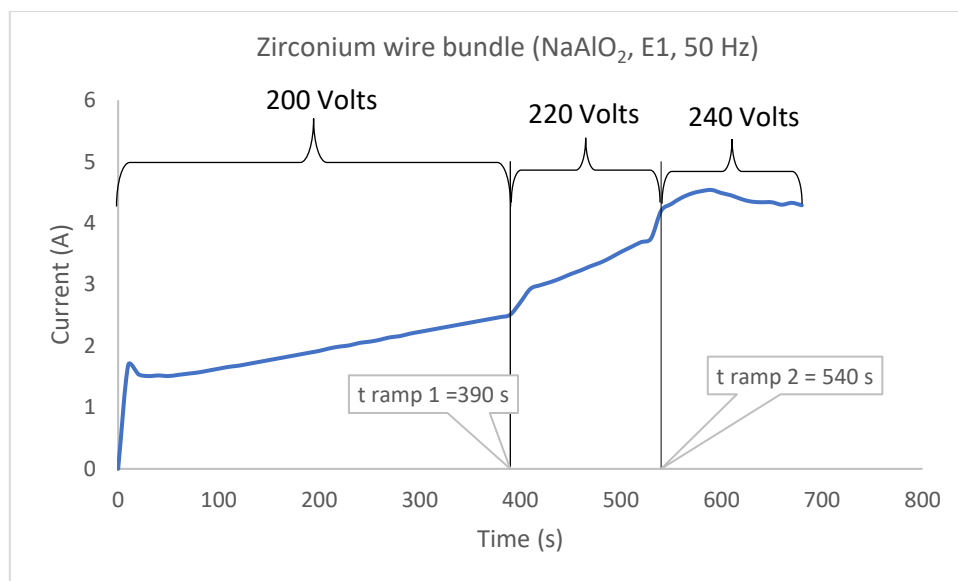
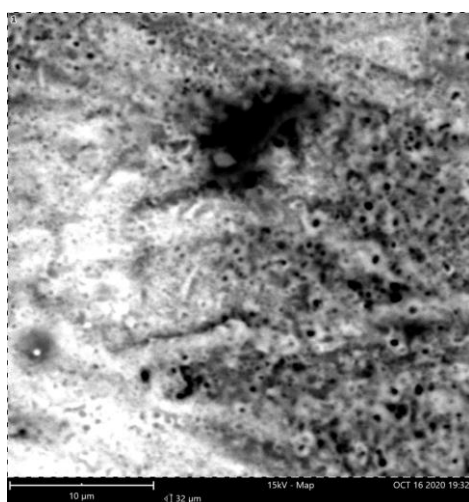


Figure 4-15 Current time graph for a Zr wire bundle sample with voltage ramps

### 4.3. SEM-EDX

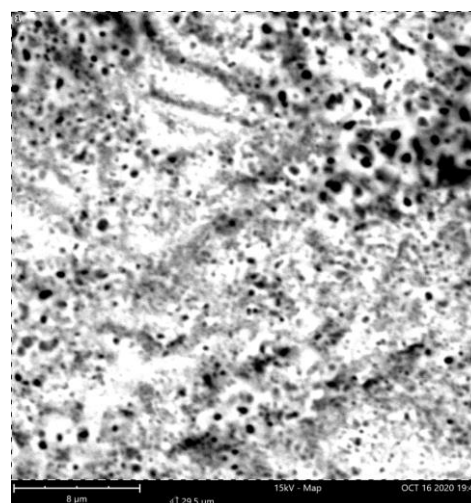
Similar to the current time data, this section is divided based on the type of samples processed. The samples were characterised using the BSD of the Phenom ProX electron microscope with 15 kV mapping and a resolution of 64 x 64 pixels.

#### a) 1 cm diameter titanium disc samples



Element Symbol	Atomic Conc.	Weight Conc.	Oxide Symbol	Stoich. wt Conc.
O	69.39	50.78		
Ti	16.97	37.14	TiO <sub>2</sub>	76.68
Si	4.41	5.67	SiO <sub>2</sub>	15.01
C	5.51	3.03		
F	2.89	2.51		
Na	0.83	0.87	Na <sub>2</sub> O	1.46

Figure 4-17 SEM-EDX for 1 cm disc (200 V, 200 Hz, Na<sub>2</sub>SiO<sub>3</sub>, E2)



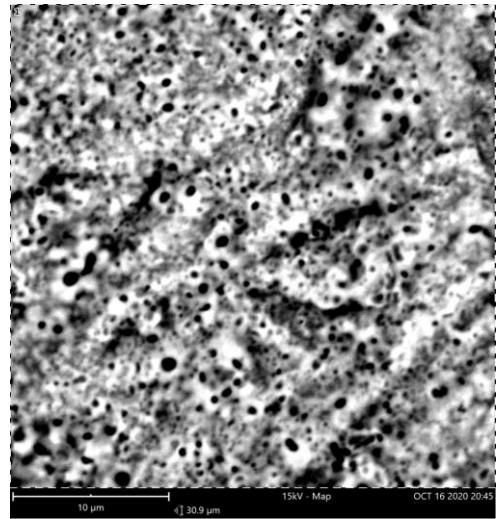
Element Symbol	Atomic Conc.	Weight Conc.	Oxide Symbol	Stoich. wt Conc.
O	71.44	50.04		
Ti	20.10	42.12	TiO <sub>2</sub>	83.34
Si	4.21	5.18	SiO <sub>2</sub>	13.15
C	3.38	1.77		
Na	0.88	0.88	Na <sub>2</sub> O	1.41

Figure 4-16 SEM-EDX for 1 cm disc (200 V, 200 Hz, Na<sub>2</sub>SiO<sub>3</sub>, E3)



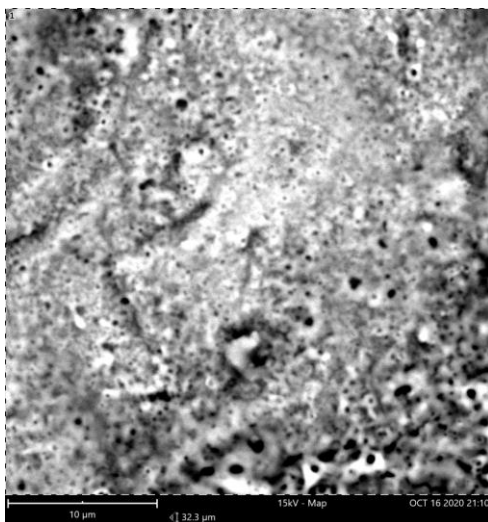
Element Symbol	Atomic Conc.	Weight Conc.	Oxide Symbol	Stoich. wt Conc.
O	71.70	50.11		
Ti	20.60	43.08	TiO <sub>2</sub>	85.73
Si	3.52	4.32	SiO <sub>2</sub>	11.03
C	3.54	1.86		
Na	0.63	0.64	Na <sub>2</sub> O	1.02

Figure 4-18 SEM-EDX for 1 cm disc (230 V, 50 Hz, Na<sub>2</sub>SiO<sub>3</sub>, E1)



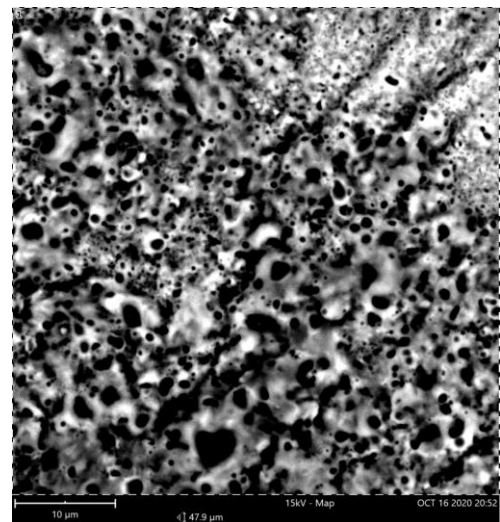
Element Symbol	Atomic Conc.	Weight Conc.	Oxide Symbol	Stoich. wt Conc.
O	75.28	53.47		
Ti	18.12	38.52	TiO <sub>2</sub>	79.71
Si	5.63	7.02	SiO <sub>2</sub>	18.64
Na	0.97	0.99	Na <sub>2</sub> O	1.65

Figure 4-19 SEM-EDX for 1 cm disc (230 V, 50 Hz, Na<sub>2</sub>SiO<sub>3</sub>, E2)



Element Symbol	Atomic Conc.	Weight Conc.	Oxide Symbol	Stoich. wt Conc.
O	74.15	52.01		
Ti	18.84	39.53	TiO <sub>2</sub>	79.03
Si	6.25	7.70	SiO <sub>2</sub>	19.74
Na	0.76	0.76	Na <sub>2</sub> O	1.23

Figure 4-20 SEM-EDX for 1 cm disc (230 V, 50 Hz, Na<sub>2</sub>SiO<sub>3</sub>, E3) - dense



Element Symbol	Atomic Conc.	Weight Conc.	Oxide Symbol	Stoich. wt Conc.
O	74.92	54.92		
Ti	14.31	31.38	TiO <sub>2</sub>	64.59
Si	10.06	12.94	SiO <sub>2</sub>	34.16
Na	0.72	0.76	Na <sub>2</sub> O	1.26

Figure 4-21 SEM-EDX for 1cm disc (230 V, 50 Hz, Na<sub>2</sub>SiO<sub>3</sub>, E3) - porous

Figures 4-16 to 21 represent the SEM-EDX results for 1 cm disc samples coated in progressively increasing voltages and electrolyte concentrations. In the captions, the bracketed values represent

the applied voltage, frequency, electrolyte type and classification. All images showed the presence of volcano shaped structures which are indicative and characteristic of PEO. Figures 4-16 and 17 and 4-18 and 19 are the results for the coatings formed under the same electrical parameters (voltage and frequency) but increasing electrolyte concentrations. It is seen from figures 4-16 to 19 that on increasing the electrolyte concentration, the atomic concentration of oxygen increases. Since the workpiece is pure titanium, the primary coating oxide will be titania ( $\text{TiO}_2$ ). The stoichiometric weight % of  $\text{TiO}_2$  increases from 76.68 to 83.34 in figures 4-16 and 17. In figures 4-18 and 19, the pores are visually observed to be larger, indicating a larger extent of coating formation. The amount of electrolyte deposition in the form of  $\text{SiO}_2$  increased from 11.03 to 18.64 weight% which resulted in the decrease in the amount of  $\text{TiO}_2$  from 85.73 to 79.71 weight%. This result is in agreement with literature which states that employing more conductive electrolytes result in thicker porous outer layers containing a larger amount of electrolyte deposition. This parameter can also be used to tune the amount of electrolyte deposited in the coating.

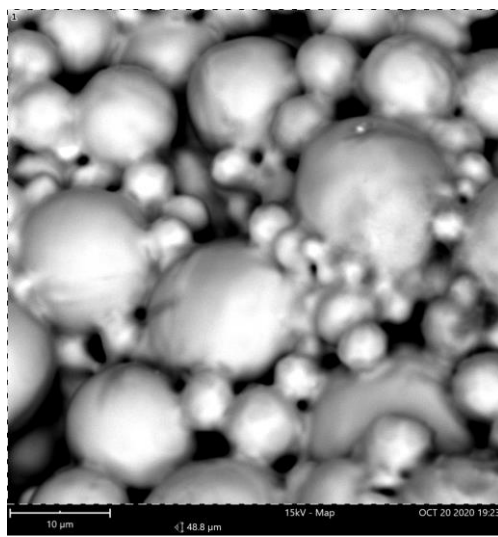
Some of the disc samples displayed visibly different morphological features over their surface. This is observed in figures 4-20 and 21 where figure 4-20 shows a region on the surface where coating has occurred to a lower extent. It is characterized by a relatively smoother surface with a high amount of  $\text{TiO}_2$  (79.03 weight%) and low amounts of electrolyte deposition (19.74 weight%  $\text{SiO}_2$ ). This type of surface is resemblant of the dense inner layer of PEO formed coatings which are directly adhered to the workpiece. In contrast, figure 4-21 shows a region on the same sample surface where extensive coating formation has taken place. The amount of  $\text{SiO}_2$  is significantly higher than the dense surface with 34.56 weight%, resulting in a lower  $\text{TiO}_2$  content of 64.59 weight%. It can also be seen that regardless of the surface being dense or porous, the oxygen content is almost the same at 74.15 and 74.92% atomic concentrations.

The presence of carbon and fluorine in some of the EDX results could be attributed to an overlap with oxygen and titanium peaks. There was no source of F in the system and hence, its presence might be that of Ti or O. At this point in experimentation, no additional elements were disabled during the EDX characterization which explains the presence of the extra elements in the EDX results.

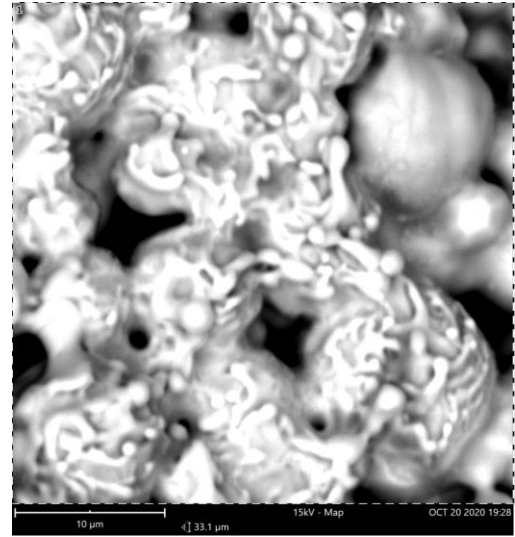
### **b) 3D printed titanium scaffold**

The SEM-EDX results of a 3D scaffold sample analyzed at two different regions (A and B) on the same sample is shown in figure 4-22. Region B shows the presence of deposition which could be the deposition of Na and Si from the electrolyte. The EDX results indicate that significant oxidation has taken place, which can be realized from the 53.55 and 51.86% atomic concentrations of oxygen on regions A and B. The same can be seen for the other elements including the oxide concentrations of

Na and Si. The only oxide component which showed a greater difference in weight was  $\text{TiO}_2$  at 92.35 and 96.31 stoichiometric weight%.



A)

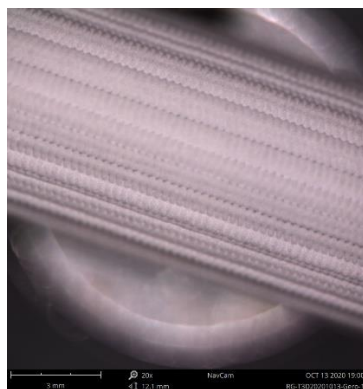


B)

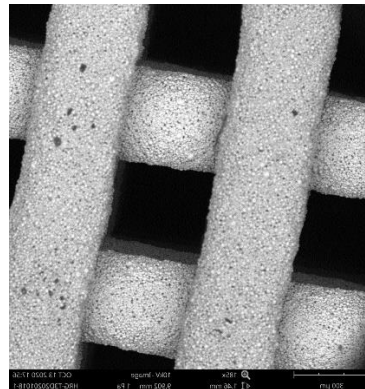
Element Symbol	Atomic Conc.	Weight Conc.	Oxide Symbol	Stoich. wt Conc.
O	53.55	28.48		
Ti	40.09	63.79	$\text{TiO}_2$	92.35
C	3.45	1.38		
Na	1.31	1.00	$\text{Na}_2\text{O}$	1.17
Si	0.69	0.64	$\text{SiO}_2$	1.19

Element Symbol	Atomic Conc.	Weight Conc.	Oxide Symbol	Stoich. wt Conc.
O	51.86	28.27		
Ti	41.92	68.37	$\text{TiO}_2$	96.31
C	4.36	1.79		
Na	1.23	0.96	$\text{Na}_2\text{O}$	1.10
Si	0.63	0.60	$\text{SiO}_2$	1.09

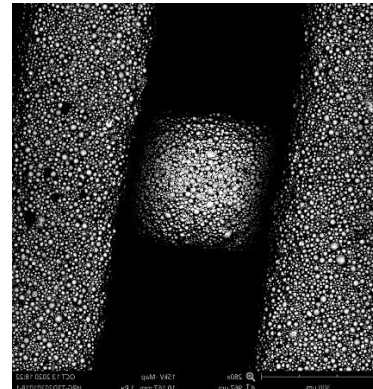
Figure 4-22 SEM-EDX for a cut 3D scaffold sample (200 V, 50 Hz,  $\text{Na}_2\text{SiO}_3$ , E1) for two different regions A and B on the same sample



A)



B)



C)

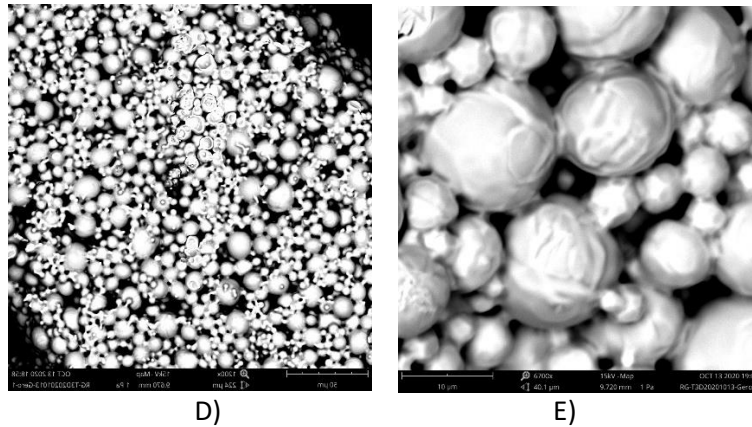
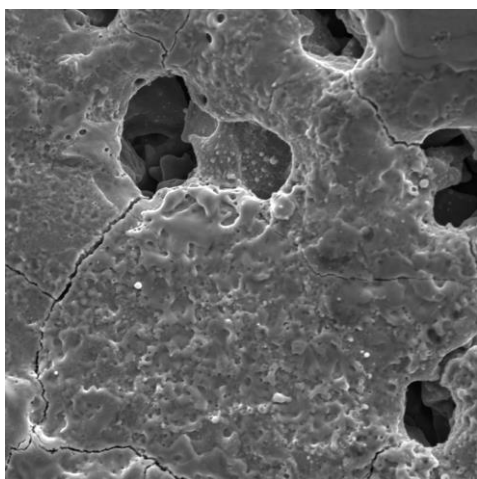


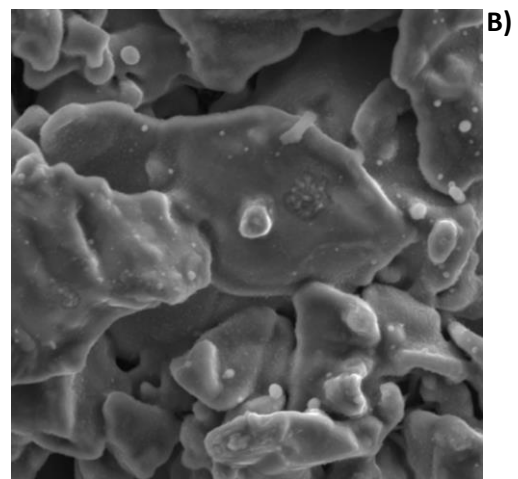
Figure 4-23 SEM images of a 3D printed scaffold A) lateral surface (20x); B) top view of the struts (185x); C) Top view (280x); D) Structure of a single strut (1200x); E) particle structure (6700x)

SEM images of a 3D scaffold sample at different magnifications are shown in figure 4-23. It can be inferred that the samples are relatively porous owing to their strut like structure (figure 4-23 B and C). Even at a microscopic level, at a map resolution of 10  $\mu\text{m}$  shown in figure 4-23 E), it is seen that there are visible gaps between the particles indicating the presence of micro porosity as well.

**c) 1 cm long porous titanium tubes**



Element Symbol	Atomic Conc.	Weight Conc.	Oxide Symbol	Stoich. wt Conc.
Ti	29.77	52.56	TiO <sub>2</sub>	91.88
O	68.29	40.29		
La	1.27	6.48		
Al	0.67	0.67	Al <sub>2</sub> O <sub>3</sub>	1.33



Element Symbol	Atomic Conc.	Weight Conc.	Oxide Symbol	Stoich. wt Conc.
Ti	35.65	62.37	TiO <sub>2</sub>	100.00
O	64.35	37.63		

Figure 4-24 SEM-EDX of 1 cm long porous Ti tubes (200 V, 50 Hz, NaAlO<sub>2</sub>, E1) for two regions A) and B) of the same sample

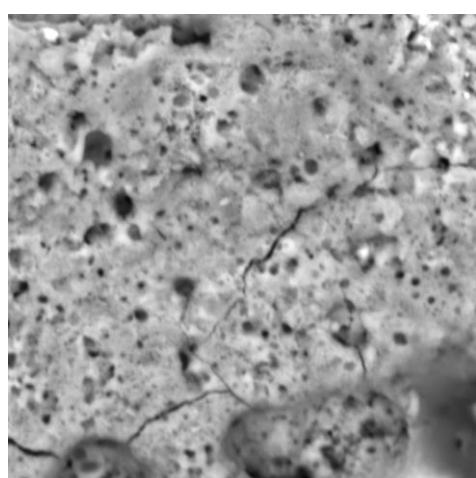
Figure 4-24 shows the SEM-EDX for a porous tube sample at two different regions on the sample surface. It is seen that the coating morphology is rather non-homogeneous with the region A) being more coated than region B). Due to the intense sparking, cracks are visible on the coated surface and can be seen in figure 4-24 A. Region B, has been coated as well, which can be inferred from the oxygen atomic concentration of 64.35% which is slightly lower than that of region A at 68.29%. It was also



observed that there was no deposition of the electrolyte on region B indicating very thin, dense coatings. The results in figure 4-24 were for a sample wound with titanium wire and immersed completely in the aluminate electrolyte. The type of connection could also be the reason for the non-homogeneous coatings as the current is first conducted by the wire and then contacts the workpiece.

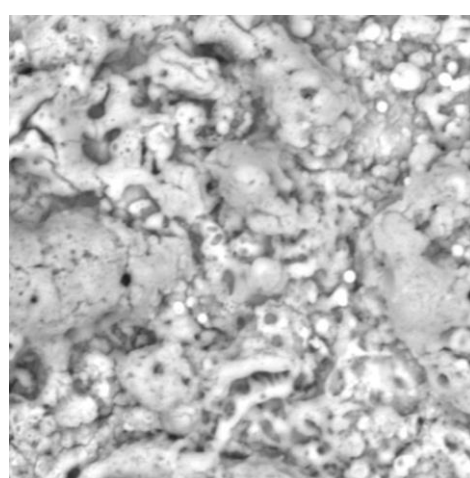
#### d) Titanium wire samples

The SEM-EDX results of samples consisting of three titanium wires are shown in figure 4-25. The results are for the samples processed in E2 of the aluminate based electrolyte. With the electrolyte being the same, the effect of increasing voltage can be realized from the figure. The applied voltage for samples A), B) and C) were 220, 240 and 260 Volts. It can be seen that the extent of oxidation increases significantly with increase the voltage. The stoichiometric weight percent of  $TiO_2$  was only 25.01%



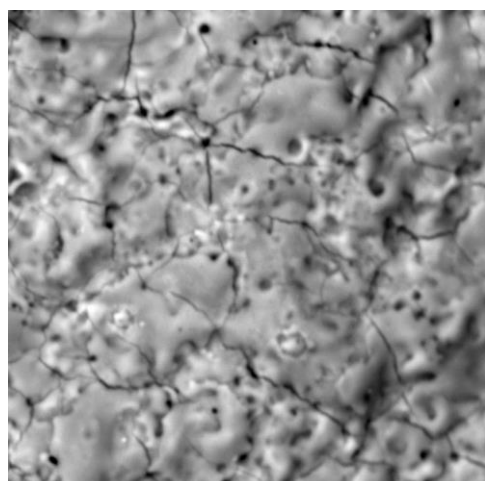
A)

Element Symbol	Atomic Conc.	Weight Conc.	Oxide Symbol	Stoich. wt Conc.
O	60.46	50.13		
Al	19.88	27.79	$Al_2O_3$	63.05
C	13.77	8.57		
Ti	5.03	12.49	$TiO_2$	25.01
Na	0.86	1.02	$Na_2O$	1.65



B)

Element Symbol	Atomic Conc.	Weight Conc.	Oxide Symbol	Stoich. wt Conc.
O	68.99	48.12		
Ti	19.00	39.65	$TiO_2$	78.08
C	4.97	2.60		
Al	4.28	5.04	$Al_2O_3$	11.24
Na	1.48	1.48	$Na_2O$	2.36
Fe	1.28	3.12	$Fe_2O_3$	5.26

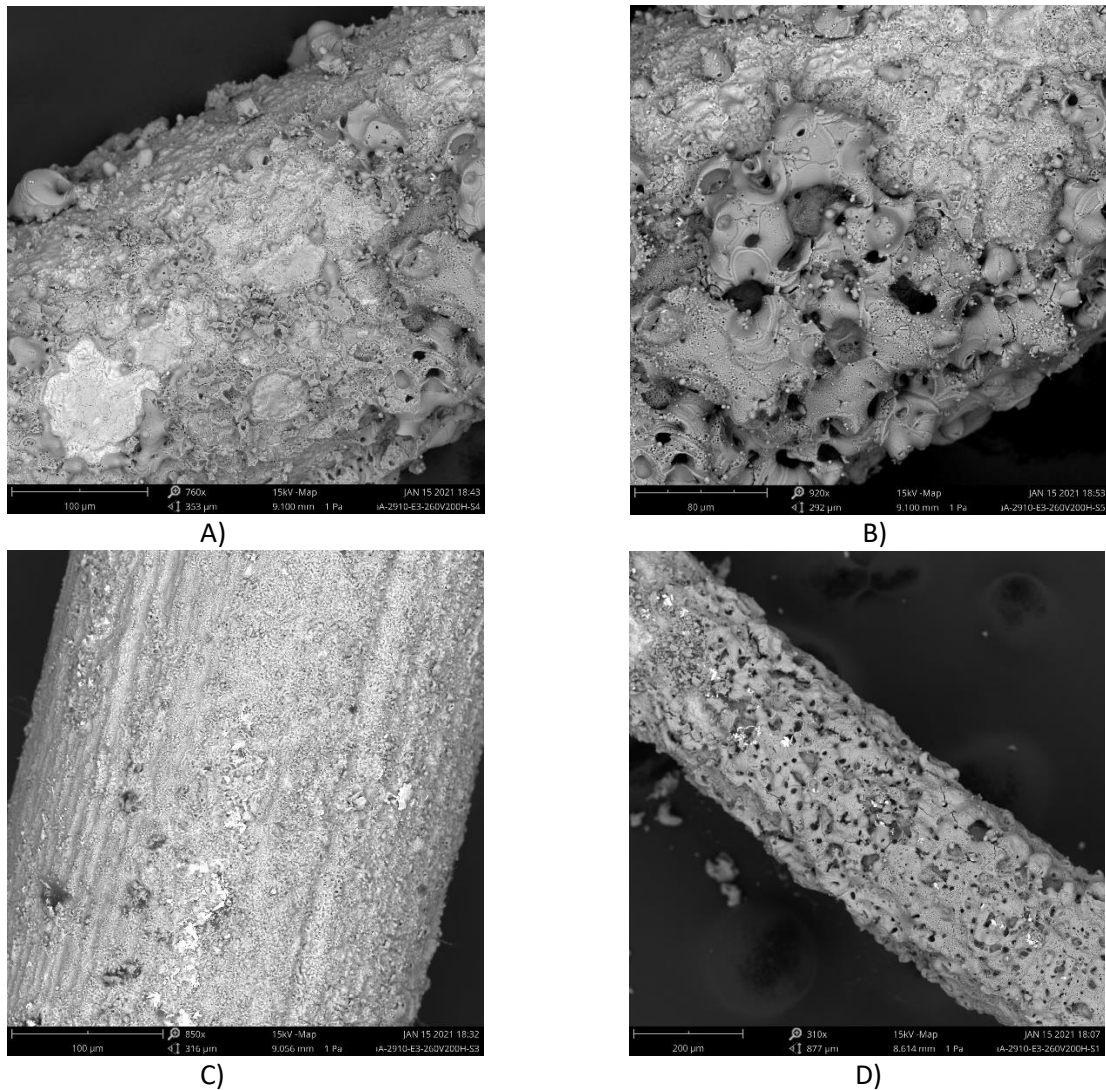


C)

Element Symbol	Atomic Conc.	Weight Conc.	Oxide Symbol	Stoich. wt Conc.
O	67.52	41.33		
Ti	31.46	57.62	$TiO_2$	97.97
Al	1.02	1.06	$Al_2O_3$	2.03

Figure 4-25 SEM-EDX for TW wire samples (50 Hz,  $NaAlO_2$ , E2) at A) 220 Volts; B) 240 Volts; C) 260 Volts

for A) but 97.97% for C) which had an applied voltage of 260 volts. The higher voltage of C) also resulted in visible cracks being formed on the coating due to more energetic discharges and currents being produced on the sample. It was also observed that increasing voltages made the surfaces smoother and less porous. This can be inferred from the electrolyte compound concentration in the coatings. Aluminum oxide ( $\text{Al}_2\text{O}_3$ ) is the primary electrolyte deposited compound as the electrolyte used is  $\text{NaAlO}_2$ . In A) the weight% of  $\text{Al}_2\text{O}_3$  is 63.05% which reduces to 11.24% in B) and 2.03% in C).



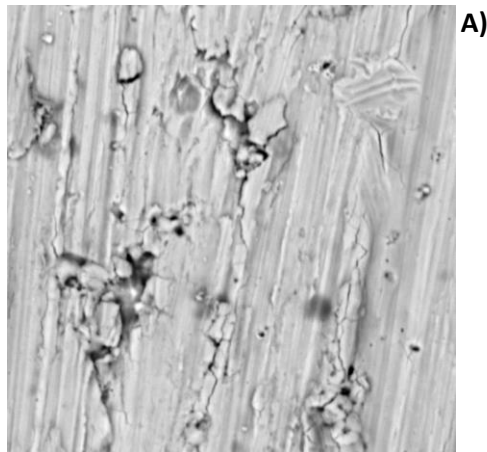
*Figure 4-26 SEM images at different regions and magnifications of a TW sample (260 V, 200 Hz,  $\text{NaAlO}_2$ , E3)*

SEM images for different regions and magnifications of a titanium wire sample are shown in figure 4-26. The morphology of the coatings are observed to be non-homogeneous. Some portions of the wire were smooth and dense (figure 45-C) while others showed regions (figure 4-26 B and D) with large amount of electrolyte component deposition. The non-homogeneity can be attributed to the high temperatures and currents generated during the process. The process was still being studied and hence it was not entirely optimal in terms of controlled electrolyte temperature and plasma discharge. The seizing and continuing of intense sparking could also be a reason for uneven coating deposition

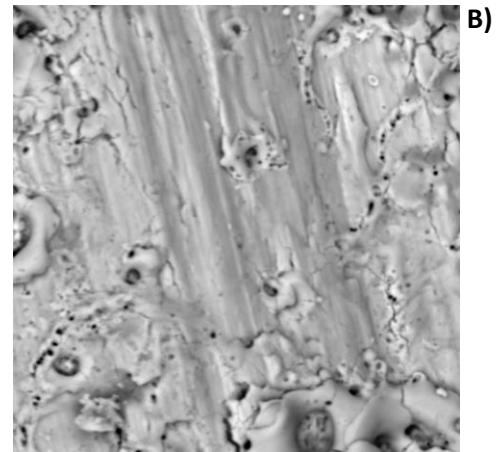
on the sample surface. However, it was found that the entire surface of the sample that was immersed in the electrolyte was coated by at least the dense inner layer, even if there was no electrolyte deposited coating.

**e) Zirconium wire and wire bundle samples**

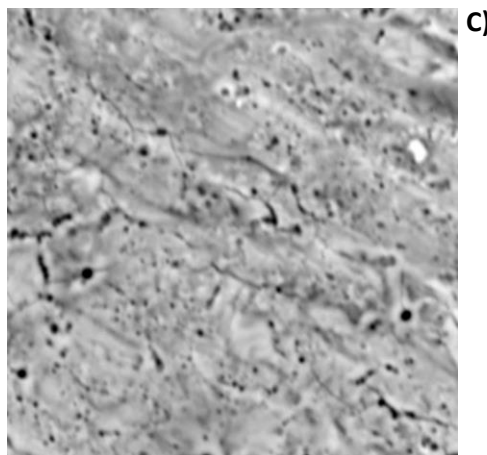
SEM-EDX results for zirconium wire samples are shown in figure 4 where the samples were processed in the aluminate electrolyte. A) and B) were treated at 220 V and C) and D) at 240 V.



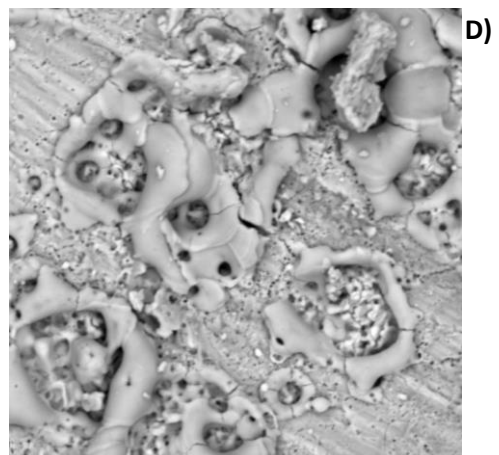
Element Symbol	Atomic Conc.	Weight Conc.
O	42.91	21.44
C	34.00	12.76
Zr	23.09	65.80



Element Symbol	Atomic Conc.	Weight Conc.
O	54.57	26.66
Zr	23.09	64.30
C	20.48	7.51
Al	1.86	1.53



Element Symbol	Atomic Conc.	Weight Conc.
O	57.12	28.67
Zr	21.35	61.11
C	16.86	6.35
Al	3.95	3.34
Na	0.72	0.52

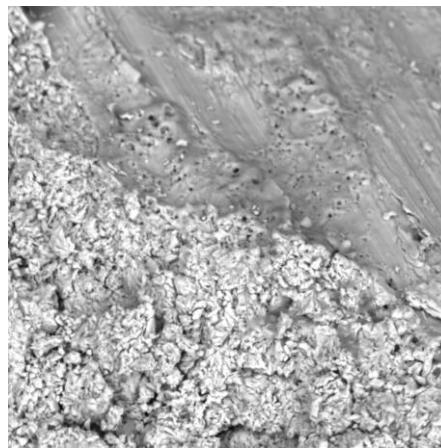
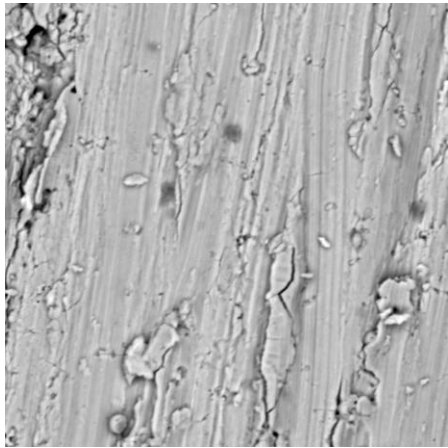


Element Symbol	Atomic Conc.	Weight Conc.
O	69.06	29.32
Zr	28.47	68.91
Al	2.48	1.77

Figure 4-27 SEM-EDX for Zr wire samples A) and B) (220 V, 50 Hz, NaAlO<sub>2</sub>, E2); C) and D) (240 V, 50 Hz, NaAlO<sub>2</sub>, E2)



The 220 V samples possessed a relatively smoother surface indicating a denser and thinner coating. From figure 4-27 C) and D), a more porous and especially in D), uneven lump like structures can be seen indicating a larger amount of Al and Na deposition from the electrolyte. Expectedly, the oxygen and Zr content increased with increasing voltage from 42.91 and 23.09% to 69.06 and 28.47% atomic concentration.



Element Symbol	Atomic Conc.	Weight Conc.
Zr	21.78	62.33
O	53.85	27.03
C	23.07	8.70
Y	0.49	1.36
Na	0.81	0.58

Element Symbol	Atomic Conc.	Weight Conc.
Zr	29.77	67.94
O	68.00	27.22
Rb	1.19	2.55
Y	1.03	2.30

Figure 4-28 SEM-EDX for Zr wire bundle sample (200 V, 50 Hz, Na<sub>2</sub>SiO<sub>3</sub>, E1)

Two regions of a Zr wire bundle sample were characterized by SEM-EDX and their results are shown in figure 4-28. Similar to the titanium wire samples, it was observed that the coatings over the entire sample surface were not fully homogeneous. The second region in figure 4-28 has been coated to a larger extent as seen by the raised, rough surface. The first region is more smooth, even and dense with a higher amount of Zr at 29.77% atomic concentration. This is an indication that the second region has a higher amount of electrolyte component deposition which is responsible for the rough and uneven surface.

For the bundle samples, Rubidium (Rb), Yttrium (Y) and a substantial amount of C (23.07% atomic concentration in region 2) were detected. In the system there was no source or possibility for Rb and Y to be present. On analyzing the EDX spectra, it was seen that the peaks of Rb and Y were very close and almost overlapped with the Zr peaks. Hence, it is very likely that the Y and Rb content account for additional Zr content on the coating.

## 4.4. XRD

### a) 1 cm diameter titanium discs

A number of disc samples were analyzed by XRD and all of them showed the presence of anatase TiO<sub>2</sub> which is one of the crystalline phases of titanium oxide. In figure 4-29, the XRD results are shown for two of the processed samples. The peak for anatase (red bar) however, is rather small indicating that not much of the oxide phase is crystalline. A more controlled process with a longer oxidation time is required to increase the crystallinity of the oxide coating and obtain stronger peaks for anatase and possibly even rutile which is desired.

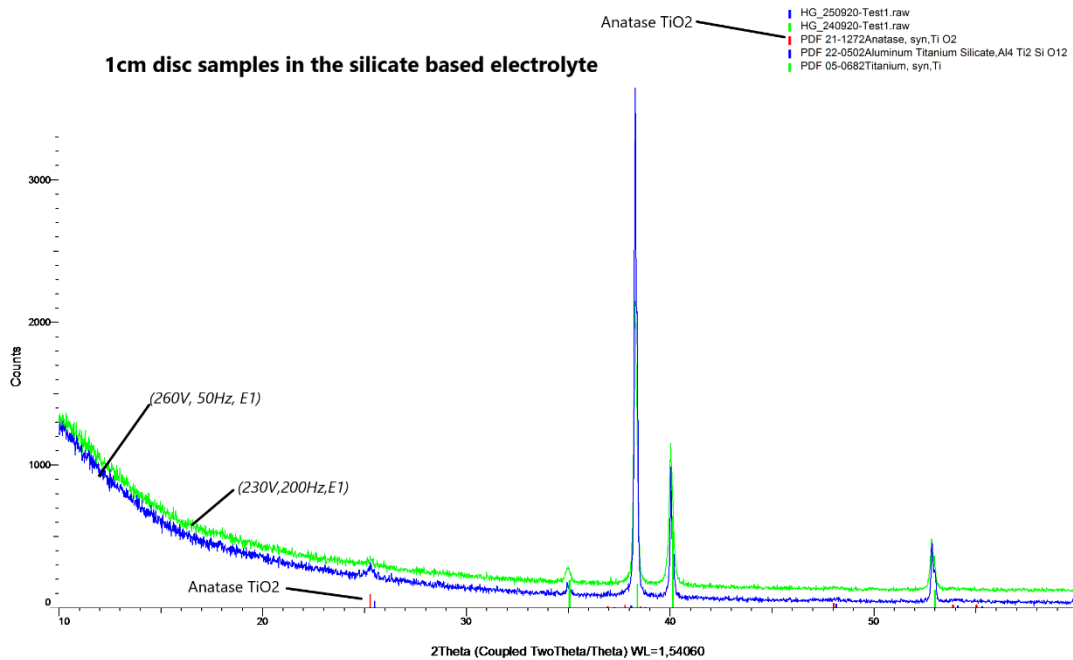


Figure 4-29 XRD for 1 cm diameter titanium disc samples

**b) 1 cm porous titanium tubes**

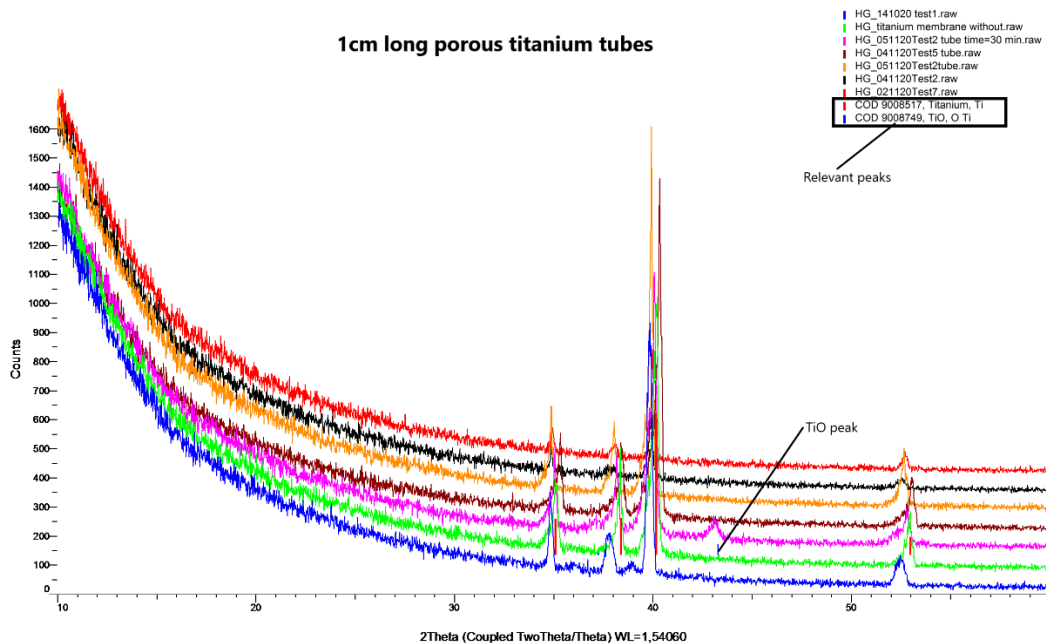


Figure 4-30 XRD for 1 cm long porous tubular samples

The XRD results shown in figure 4-30 indicate that the only oxide present on the coated tube samples is TiO which is not a crystalline phase of titania. This implies that the process parameters such as voltage, current and oxidation time were not sufficient to form crystalline phases of TiO<sub>2</sub>. A possible reason for this can be ascribed to the current limit of the power source. Due to the comparatively larger surface area of the tube samples, the current required to obtain a conventional current-time trend with plasma discharge was more than the 6.5 A limit of the power source. Therefore, it would be necessary to use a more powerful power source with a larger output current in order to efficiently coat such samples by PEO.

### c) 3D printed titanium scaffold

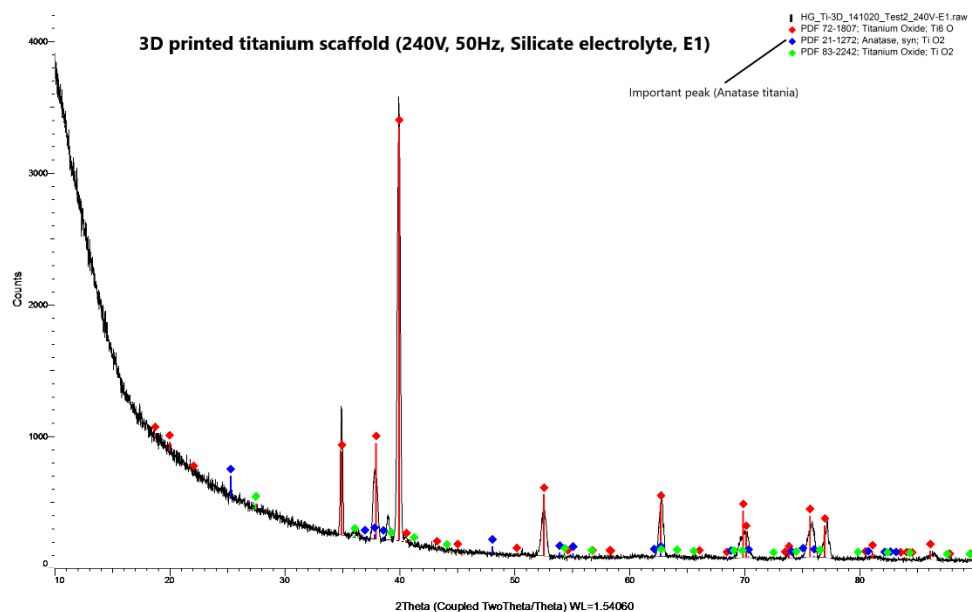


Figure 4-31 XRD for 3D printed titanium scaffold

The XRD for a 3D titanium scaffold sample is shown in figure 4-31. It showed peaks corresponding to anatase TiO<sub>2</sub> (blue lines) which is desirable. A metastable Titania phase (green line) was also present which indicates that not all the TiO<sub>2</sub> in the coating is in the crystalline phase. A longer process time with controlled discharges would result in a more crystalline TiO<sub>2</sub> than amorphous.

### d) Titanium wire bundle

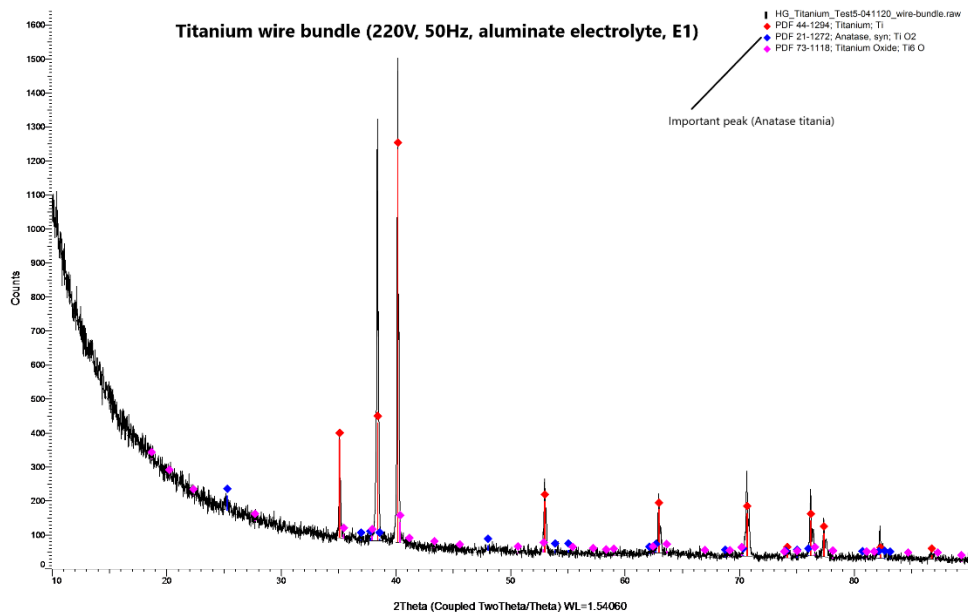


Figure 4-32 XRD for titanium wire bundle samples

The XRD for the titanium wire bundle sample shown in figure 4-32 indicated that anatase  $\text{TiO}_2$  which is desired is present in the coating although its peaks (dark blue) are very mild. Another phase of titanium oxide ( $\text{Ti}_6\text{O}$ ) represented by the pink line is present in the coating as well. The presence of anatase is a good indication that the PEO process was successfully performed on wire bundle samples, even though the process was not optimum. With fine tuning of the process parameters and better control over the electrolyte temperature, it would be possible to obtain coatings with more prominent anatase peaks resulting in higher degree of crystallinity.

#### e) Zirconium wire bundles

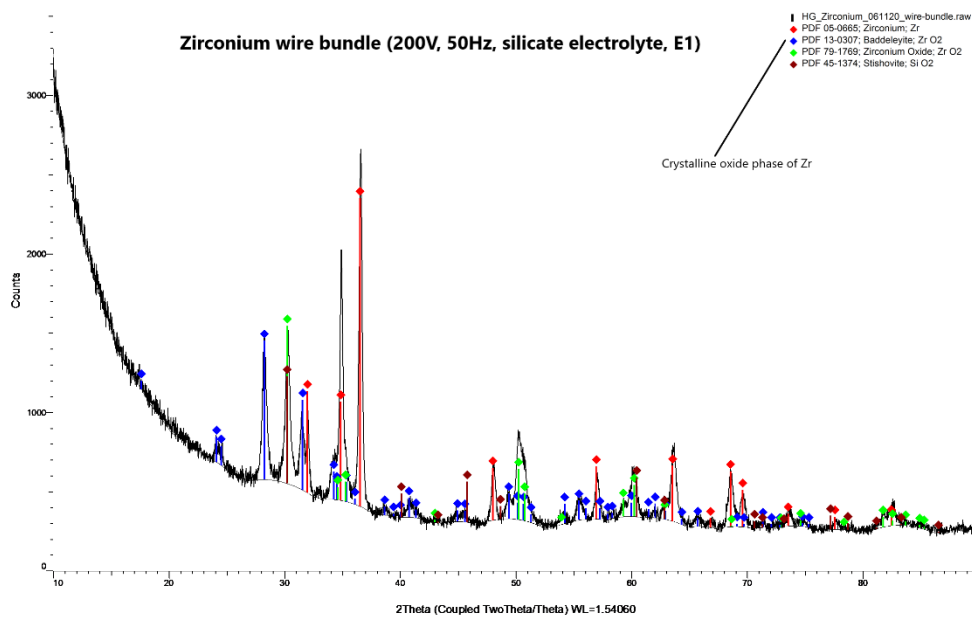


Figure 4-33 XRD for zirconium wire bundle samples

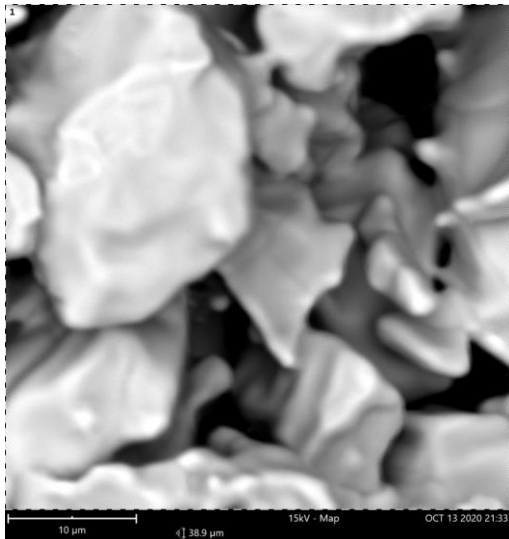
The XRD spectrum for a zirconium wire bundle sample shown in figure 4-33, has a number of peaks (blue and green) indicating a significant amount of oxidation. This result can be correlated to the experimental observations where the currents produced during the coating process were lower for Zr compared to Ti and mild spark discharge was observed on the surface. As a result, the process could be run for longer periods of time under a controlled mild-spark discharge regime which could be responsible for the relatively intense  $ZrO_2$  peaks.

Besides  $ZrO_2$ , mild peaks of  $SiO_2$  (brown lines) were also present which implies that a crystalline phase of  $SiO_2$  which is an electrolyte deposited component is present in the coating along with crystalline  $ZrO_2$ .

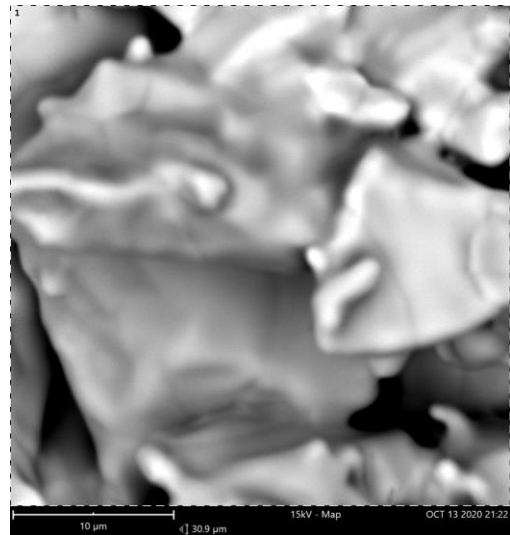
#### 4.5. Comparison between coated and non-coated samples

Figures 4-34 to 38 show an SEM-EDX comparison for coated and non-coated samples. This is performed as a check to determine whether oxidation has occurred by PEO. The images and data on the left of each figure represent the uncoated or fresh sample and those on the right are for a coated sample of the same type. Samples that were fabricated by high temperature sintering such as the porous tubes show some amount of oxidation even in the fresh state which could be attributed to oxidation at those high temperatures. However, after treatment, it is seen the oxygen atomic concentration is significantly higher for those sample types thereby confirming that oxidation by PEO has taken place. The difference in morphology for the titanium wire, zirconium wire and 1cm disc samples is another indicator of PEO. The aforementioned coated samples possess volcano or pancake like structures which is a characteristic feature of PEO formed coatings.

Due to the porous structure of the tube and 3D printed samples (figures 4-34 and 35), there was no evident difference between the coated and non-coated sample morphology. For these samples, the oxidation is confirmed by the EDX data and it is seen that on processing, similar to the other sample types, there is a significant increase in oxygen content along the presence of electrolyte deposited components as well.

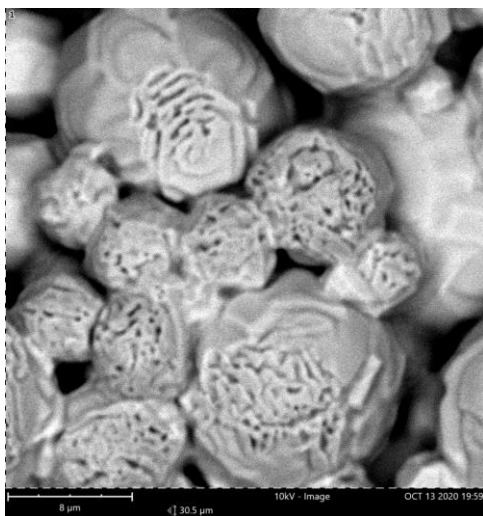


Element Symbol	Atomic Conc.	Weight Conc.
Ti	71.38	88.78
O	22.04	9.16
C	6.59	2.06

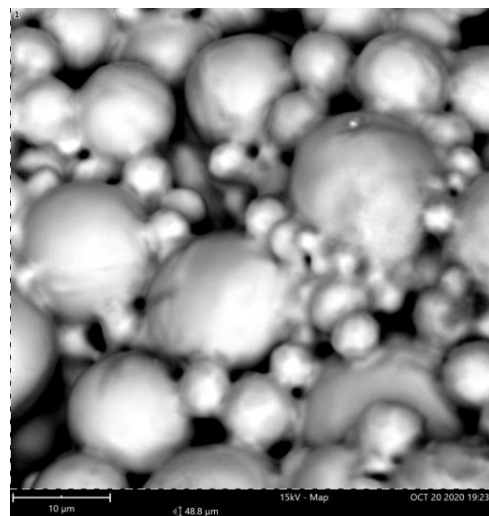


Element Symbol	Atomic Conc.	Weight Conc.	Oxide Symbol	Stoich. wt Conc.
Ti	46.89	69.34	TiO <sub>2</sub>	93.17
O	46.75	23.11		
La	0.93	4.01		
C	4.15	1.54		
In	0.34	1.19		
Si	0.94	0.82	SiO <sub>2</sub>	1.41

Figure 4-34 SEM-EDX for left) Uncoated; right) Coated 1 cm porous titanium tube sample

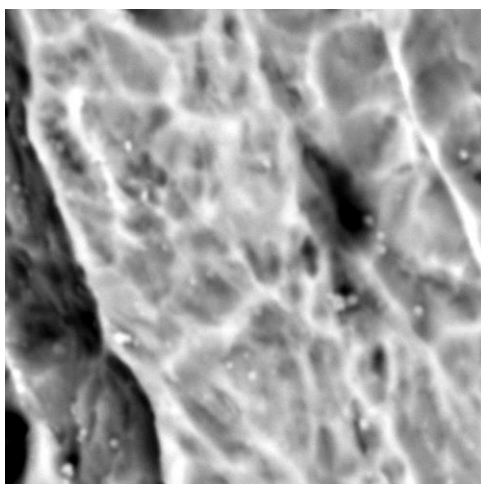


Element Symbol	Atomic Conc.	Weight Conc.
Ti	90.43	97.41
C	9.57	2.59

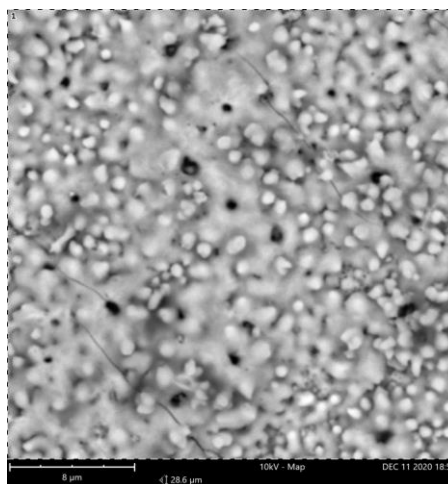


Element Symbol	Atomic Conc.	Weight Conc.	Oxide Symbol	Stoich. wt Conc.
O	53.55	28.48		
Ti	40.09	63.79	TiO <sub>2</sub>	92.35
C	3.45	1.38		
Na	1.31	1.00	Na <sub>2</sub> O	1.17
Si	0.69	0.64	SiO <sub>2</sub>	1.19

Figure 4-35 SEM-EDX for left) Uncoated; right) Coated 3D printed titanium scaffold

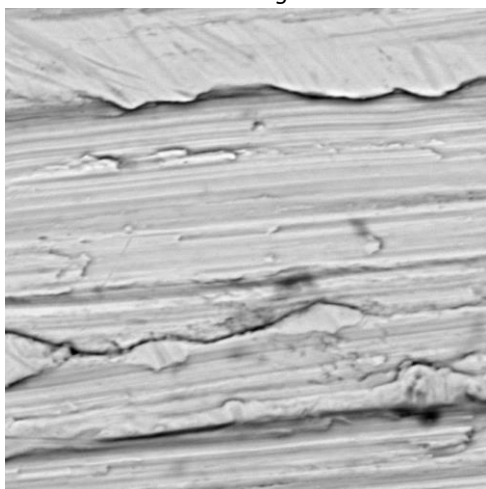


Element Symbol	Atomic Conc.	Weight Conc.
Ti	77.26	93.12
C	22.74	6.88

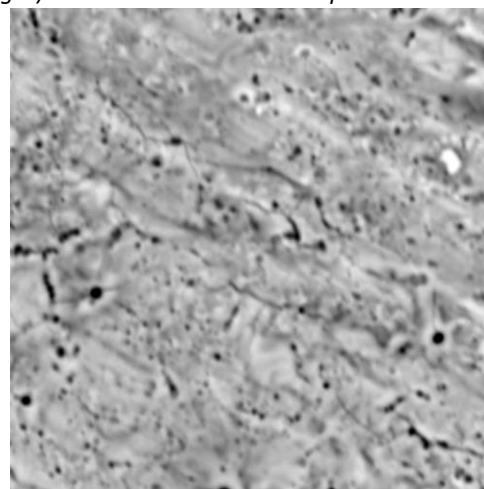


Element Symbol	Atomic Conc.	Weight Conc.	Oxide Symbol	Stoich. wt Conc.
O	68.58	52.76		
Ti	13.68	31.49	TiO <sub>2</sub>	70.66
C	11.84	6.84		
Al	3.88	5.03	Al <sub>2</sub> O <sub>3</sub>	12.79
Fe	1.04	2.79	Fe <sub>2</sub> O <sub>3</sub>	5.37
Na	0.99	1.09	Na <sub>2</sub> O	1.98

Figure 4-36 SEM-EDX for left) Uncoated; right) Coated titanium wire sample

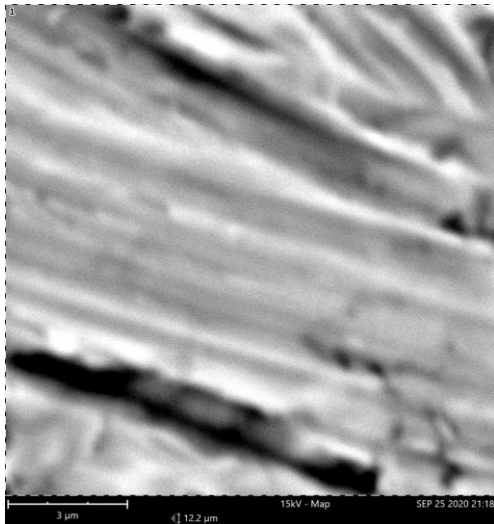


Element Symbol	Atomic Conc.	Weight Conc.
Zr	52.52	85.88
C	44.60	9.60
Y	1.75	2.79
Rb	1.13	1.73



Element Symbol	Atomic Conc.	Weight Conc.	Oxide Symbol	Stoich. wt Conc.
O	57.12	28.67		
Zr	21.35	61.11		
C	16.86	6.35		
Al	3.95	3.34	Al <sub>2</sub> O <sub>3</sub>	8.48
Na	0.72	0.52	Na <sub>2</sub> O	0.94

Figure 4-37 SEM-EDX for left) Uncoated; right) Coated zirconium wire sample



Element Symbol	Atomic Conc.	Weight Conc.
Ti	86.89	96.35
C	13.11	3.65



Element Symbol	Atomic Conc.	Weight Conc.	Oxide Symbol	Stoich. wt Conc.
O	71.70	50.11		
Ti	20.60	43.08	TiO <sub>2</sub>	85.73
Si	3.52	4.32	SiO <sub>2</sub>	11.03
C	3.54	1.86		
Na	0.63	0.64	Na <sub>2</sub> O	1.02

Figure 4-38 SEM-EDX for left) Uncoated; right) Coated 1 cm diameter titanium disc sample

## 4.6. Coating thickness

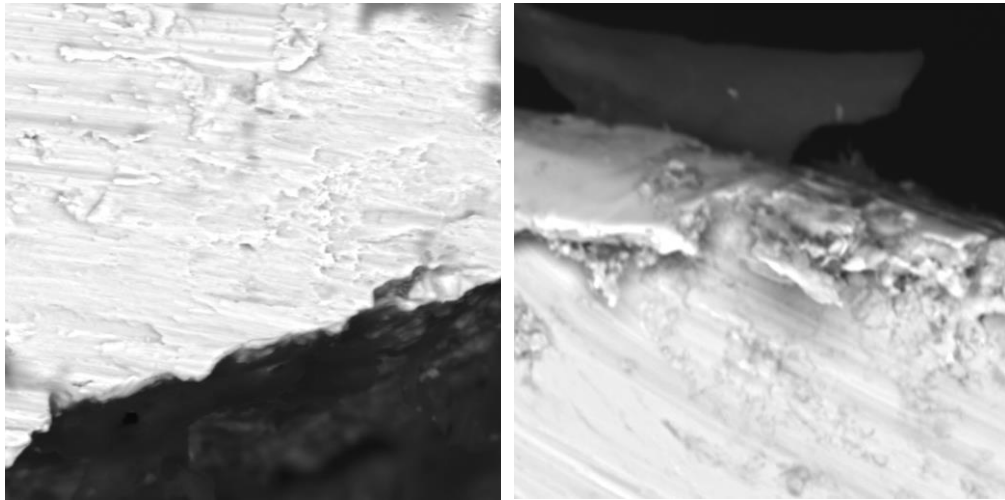
To determine the thickness the coatings, it was necessary to obtain cross sectional pieces of the coated samples and analyse them by SEM. An attempt was made to obtain cross sections of the coated 1 cm diameter titanium disc samples by cryogenic fracturing; which is a process by which the coated sample is immersed in liquid nitrogen to make it more brittle. This enables the sample to shatter easily on application of a strong impulse force on its surface. When this technique was applied to the disc samples, it was observed that due to the thickness of the sample and the inert hardness of titanium as a metal, it was not possible to break the disc samples into cross sections. The amount of force required to shatter the samples was more than that which could be supplied by physical striking.

Therefore, a cross sectional sample was taken of a coated titanium wire and is shown in figure 4-39. It was mechanically easier to cut the wire as it was only 300 μm in diameter and could be sliced using a sharp blade. The cross sectional sample was characterised by SEM to determine if there was any



visual difference between the sample and the coating which can be seen if the formed coatings are thick enough [48].

It can be seen from figure 4-39 that there is no such distinction indicating that the thickness of the coating layer is not enough to be detected by SEM and hence the coating thickness could not be quantified.

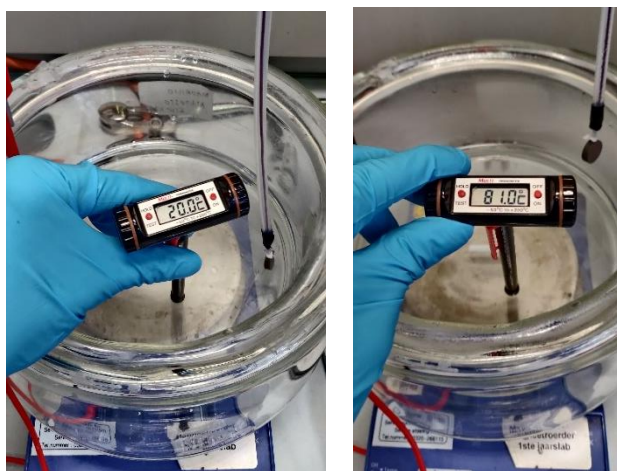


*Figure 4-39 Cross sectional SEM image of a coated titanium wire sample*

## 4.7. Electrolyte temperature

One of the process parameters in PEO which is vital to obtain thick, homogenous and strongly adherent coatings is the electrolyte temperature [49]. In general, the optimum range of electrolyte temperature in PEO varies in literature but the most common temperature range is from 20 to 40 °C. Higher electrolyte temperatures result in a reduction of the coating thickness and growth rate and also produce coatings that are poorly adhered to the workpiece.

It was observed that during experimentation, the amount of heat generated by plasma discharge and localized heating around the sample was more than what the cooling system was capable of cooling, resulting in end temperatures of the electrolyte being greater than 65 °C. Figure 4-40 shows a comparison of electrolyte temperatures measured prior and after an experimental run. At that stage, cooling was not employed and the electrolyte temperature was found to reach 81 °C. On addition of the cooling system, the electrolyte temperatures were found to be a little lower, in the range of 65 – 75 °C but still above the maximum optimal value of 40 °C. It is therefore imperative to modify the cooling system to optimize cooling of the electrolyte and maintain its temperature within the optimal range.



*Figure 4-40 Electrolyte temperature measured before and after an experimental run*

## 5. Conclusions

Five types of samples with different geometric configurations were processed by plasma electrolytic oxidation. During experimentation, intense spark discharge was observed for all the samples being processed, indicating that the applied voltage was above the breakdown voltage of the material and was sufficient to initiate PEO. Process parameters such as applied voltage, frequency and electrolyte concentration were varied, including the use of a second electrolyte ( $\text{NaAlO}_2$ ) toward the later part of experimentation.

The process parameters play an important role in the structure and composition of the coatings. With increasing voltage (200 - 260 V), the electrolyte deposition on the coatings increase, thereby increasing the coating thickness. As a result, the porosity of the coatings increase as well. A similar effect was observed for the electrolyte concentration. For the most dilute electrolyte E1 of both  $\text{Na}_2\text{SiO}_3$  and  $\text{NaAlO}_2$ , the extent of oxidation was the lowest and the current produced were correspondingly low. Hence, for dilute electrolytes, it was possible to apply higher voltages without the current reaching the maximum set value of 6.5 A. With increasing electrolyte concentrations (E2 and E3), the oxygen content in the coatings increased along with the output current as observed in EDX and current-time data. Therefore, the electrolyte concentration and applied voltage, especially in a Potentiostatic process, sets the limit to the size of the samples that can be processed. This is due to the fact that the sample's surface area is directly proportional to the current generated.

SEM-EDX were performed for a few samples of every type and it was observed that all the samples except for the 1 cm long porous tube samples showed the presence of anatase  $\text{TiO}_2$  which is a crystalline oxide phase of Ti and desirable for the scope of this work. The tubular samples showed the presence of a non-crystalline TiO phase indicating that the amount of oxidation on those samples was not sufficient to form crystalline phases like anatase or rutile in the coating.

Confirmation of coating by PEO for the scope of this work can be realized by the combination of SEM-EDX, XRD and visual results. The contribution of SEM-EDX is the presence of pancake like structures indicating porosity coupled with the high oxygen content from the EDX data. XRD results indicated that most of the samples possessed anatase as a crystalline phase which was desired and one of the aims of this work. The occurrence and presence of intense sparking on the samples during treatment was observed visually which is a phenomenon unique to PEO and which sets it apart from other similar electrochemical techniques like anodization.

The applications for this work were PEO for catalyst and membrane applications. The application for catalyst systems is promising as the coatings formed by PEO can be used as a support for catalyst layer deposition and impregnation. Furthermore, the coating composition can be fine-tuned to obtain desired concentrations of electrolyte deposited compounds by varying the applied voltage, electrolyte

concentration and type of electrolyte. Even though the coatings produced during this work was not completely optimal, it serves as a strong foundation for tailoring the process in the future to obtain coatings with desired properties of pore size, thickness and density. A viable candidate for the catalytic application was found to be the wire samples, owing to their small surface area, ease of handling and possibility of processing multiple samples at the time, for example, as bundles.

The porous tube samples were used as a base for study in membrane applications. However, due to its geometry and larger surface area, processing these samples by PEO was complicated. When wrapping the tube samples with wire and immersing it in the electrolyte, the entire sample was exposed to the electrolyte solution and could be coated. The electrical connection to the sample was not optimum since the current was conducted by the wire which in turns contacted the tube sample. Therefore, even though spark discharge was observed on the tube samples, the extent of oxidation was unsatisfactory as indicated by XRD. Hence, it can be concluded that PEO for membrane applications warrants more work, research and time to be viable, at least for the scope of this work.

## 6. Recommendations for future work

The recommendations for future work with regard to the application of PEO for catalyst and membrane applications entail tuning the process parameters to obtain satisfactory coatings based on all the results and observations from this work.

To control and maintain the temperature of the electrolyte with the optimal range of 20 – 40 °C, a more powerful cooling system would need to be utilised. This would not only maintain the electrolyte temperature but also enable the process to be performed for longer periods of time, thereby adding oxidation (process) time as a controlled variable. This would also enable the tailoring of coating thickness by increasing and decreasing the process time as required.

More optimal sample holders can be devised based on the samples being processed. This would result in more efficient electrical contact between the power source and the workpiece. This is especially crucial for processing samples with complex geometry, such as the tubes. Based on current-time and XRD data, it is evident that the power sourced used in this work is not adequate to coat samples with large surface areas like those of the tubes. Therefore, for the continuation of research on PEO for membrane applications, a more powerful power source with a higher current rating would be required.

## 7. References

- [1] G. P. Wirtz, S. D. Brown, and W. M. Kriven, "Ceramic coatings by anodic spark deposition," *Mater. Manuf. Process.*, vol. 6, no. 1, pp. 87–115, Jan. 1991.
- [2] R. S. Wernick; Pinner, "The surface treatment and finishing of aluminium and its alloys. Fourth Edition. Volume 1," p. 1273, 1972.
- [3] J. Donaldson Craig, "Anodic Oxidation of Aluminium and its Alloys," *J. R. Aeronaut. Soc.*, vol. 42, no. 331, pp. 603–612, 1938.
- [4] H. Wolters, H. Van Daltsen, and J. Metz "Method for producing a membrane and such membrane," Jan. 2011.
- [5] H. R. Godini, A. Gili, O. Görke, U. Simon, K. Hou, and G. Wozny, "Performance analysis of a porous packed bed membrane reactor for oxidative coupling of methane: Structural and operational characteristics," *Energy and Fuels*, vol. 28, no. 2, pp. 877–890, Feb. 2014.
- [6] Y. H. Ma, W. R. Moser, A. G. Dixon, A. M. Ramachandra, Y. Lu, and C. C. Binkerd, "Oxidative coupling of methane using inorganic membrane reactors," Federal Energy Technology Center (U.S.), Pittsburgh, PA, and Morgantown, WV, Apr. 1998.
- [7] S. Liu, X. Tan, K. Li, and R. Hughes, "Methane coupling using catalytic membrane reactors," *Catal. Rev.*, vol. 43, no. 1–2, pp. 147–198, May 2001.
- [8] F. C. Walsh, C. T. J. Low, R. J. K. Wood, K. T. Stevens, J. Archer, A. R. Poeton and A. Ryder, "Plasma electrolytic oxidation (PEO) for production of anodised coatings on lightweight metal (Al, Mg, Ti) alloys," *Transactions of the Institute of Metal Finishing*, vol. 87, no. 3. pp. 122–135, 18-May-2009.
- [9] B. Zhu, M. Duke, L. F. Dumée, A. Merenda, E. d. Ligneris, L. Kong, P. D. Hodgson and S. Gray, "Short review on porous metal membranes—Fabrication, commercial products, and applications," *Membranes*, vol. 8, no. 3. Multidisciplinary Digital Publishing Institute (MDPI), 18-Sep-2018.
- [10] L. Y. Jiang and N. Li, "Membrane-based separations in metallurgy: Principles and applications," 2017.
- [11] T. Westermann and T. Melin, "Flow-through catalytic membrane reactors-Principles and applications," *Chemical Engineering and Processing: Process Intensification*, vol. 48, no. 1. Elsevier, pp. 17–28, 01-Jan-2009.
- [12] S. Sridhar, A. Viswanathan, K. Venkateswarlu, N. Rameshbabu, and N. L. Parthasarathi, "Enhanced visible light photocatalytic activity of P-block elements (C, N and F) doped porous TiO<sub>2</sub> coatings on Cp-Ti by micro-arc oxidation," *J. Porous Mater.*, vol. 22, no. 2, pp. 545–557, 2015.

- [13] D. Quintero, O. Galvis, J. A. Calderón, J. G. Castaño, and F. Echeverría, "Effect of electrochemical parameters on the formation of anodic films on commercially pure titanium by plasma electrolytic oxidation," *Surf. Coatings Technol.*, vol. 258, pp. 1223–1231, Nov. 2014.
- [14] S. Aliasghari, P. Skeleton, and G. E. Thompson, "Plasma electrolytic oxidation of titanium in a phosphate/silicate electrolyte and tribological performance of the coatings," *Appl. Surf. Sci.*, vol. 316, no. 1, pp. 463–476, Oct. 2014.
- [15] V. Dehnavi, B. L. Luan, D. W. Shoosmith, X. Y. Liu, and S. Rohani, "Effect of duty cycle and applied current frequency on plasma electrolytic oxidation (PEO) coating growth behavior," *Surf. Coatings Technol.*, vol. 226, pp. 100–107, Jul. 2013.
- [16] L. Wang, L. Shi, J. Chen, Z. Shi, L. Ren, and Y. Wang, "Biocompatibility of Si-incorporated TiO<sub>2</sub> film prepared by micro-arc oxidation," *Mater. Lett.*, vol. 116, pp. 35–38, 2014.
- [17] S. Di, Y. Guo, H. Lv, J. Yu, and Z. Li, "Microstructure and properties of rare earth CeO<sub>2</sub>-doped TiO<sub>2</sub> nanostructured composite coatings through micro-arc oxidation," *Ceram. Int.*, vol. 41, no. 5, pp. 6178–6186, Jun. 2015.
- [18] W. Ping, W. Ting, P. Hao, and G. X. Yang, "Effect of NaAlO<sub>2</sub> concentrations on the properties of micro-arc oxidation coatings on pure titanium," *Materials Letters*, vol. 170. Elsevier B.V., pp. 171–174, 01-May-2016.
- [19] Y. Yang and H. Wu, "Effects of Current Density on Microstructure of Titania Coatings by Micro-arc Oxidation," *J. Mater. Sci. Technol.*, vol. 28, no. 4, pp. 321–324, Apr. 2012.
- [20] H. Li and J. Zhang, "Preparation of a Modified Micro-arc Oxidation Coating Using Al<sub>2</sub>O<sub>3</sub> Particles on Ti6Al4V," *J. Mater. Sci. Eng.*, vol. 06, no. 06, 2017.
- [21] Y. Xu, Z. Yao, F. Jia, Y. Wang, Z. Jiang, and H. Bu, "Preparation of PEO ceramic coating on Ti alloy and its high temperature oxidation resistance," *Curr. Appl. Phys.*, vol. 10, no. 2, pp. 698–702, Mar. 2010.
- [22] F. Jin, P. K. Chu, K. Wang, J. Zhao, A. Huang, and H. Tong, "Thermal stability of titania films prepared on titanium by micro-arc oxidation," *Mater. Sci. Eng. A*, vol. 476, no. 1–2, pp. 78–82, Mar. 2008.
- [23] Y. Yan, J. Sun, Y. Han, D. Li, and K. Cui, "Microstructure and bioactivity of Ca, P and Sr doped TiO<sub>2</sub> coating formed on porous titanium by micro-arc oxidation," *Surf. Coatings Technol.*, vol. 205, no. 6, pp. 1702–1713, Dec. 2010.
- [24] X. P. Fan, "Effects of process parameters on microarc oxidation film layers of porous titanium," *Appl. Ecol. Environ. Res.*, vol. 17, no. 4, pp. 8631–8641, 2019.
- [25] Y. W. Kim and T. H. Nam, "Surface analysis of micro-arc oxidized coatings deposited on cp-Ti,"

- Mod. Phys. Lett. B*, vol. 23, no. 31–32, pp. 3717–3723, Dec. 2009.
- [26] Y. Han, S. H. Hong, and K. W. Xu, “Porous nanocrystalline titania films by plasma electrolytic oxidation,” *Surf. Coatings Technol.*, vol. 154, no. 2–3, pp. 314–318, May 2002.
- [27] M. Shirkhazadeh, “Fabrication and characterization of alkoxy-derived nanophase TiO<sub>2</sub> coatings,” *Nanostructured Mater.*, vol. 5, no. 1, pp. 33–40, Jan. 1995.
- [28] K. W. X. Y. Han, “Structural Characterization of Micro-arc Oxidation Formed Titanium Dioxide Films Containing Ca and P,” *Journal of inorganic materials*, 2001.
- [29] J. Liu, X. Zhu, Z. Huang, S. Yu, and X. Yang, “Characterization and property of microarc oxidation coatings on open-cell aluminum foams,” *J. Coatings Technology Res.*, vol. 9, no. 3, pp. 357–363, May 2012.
- [30] N. Movahedi and A. Habibolahzadeh, “Effect of plasma electrolytic oxidation treatment on corrosion behavior of closed-cell Al-A356 alloy foam,” *Mater. Lett.*, vol. 164, pp. 558–561, Feb. 2016.
- [31] T. Abdulla, A. Yerokhin, and R. Goodall, “Effect of Plasma Electrolytic Oxidation coating on the specific strength of open-cell aluminium foams,” *Mater. Des.*, vol. 32, no. 7, pp. 3742–3749, Aug. 2011.
- [32] T. Abdulla, A. Yerokhin, and R. Goodall, “Enhancement in specific strength of open cell aluminium foams through plasma electrolytic oxidation treatment,” *Scr. Mater.*, vol. 75, pp. 38–41, Mar. 2014.
- [33] J. M. Rúa, A. A. Zuleta, J. Ramírez, and P. Fernández-Morales, “Micro-arc oxidation coating on porous magnesium foam and its potential biomedical applications,” *Surf. Coatings Technol.*, vol. 360, pp. 213–221, Feb. 2019.
- [34] K. Korkmaz, “The effect of Micro-arc Oxidation treatment on the microstructure and properties of open cell Ti6Al4V alloy foams,” *Surf. Coatings Technol.*, vol. 272, pp. 72–78, Jun. 2015.
- [35] Z. Gorgin Karaji, R. Hedayati, B. Pouran, I. Apachitei, and A. A. Zadpoor, “Effects of plasma electrolytic oxidation process on the mechanical properties of additively manufactured porous biomaterials,” *Mater. Sci. Eng. C*, vol. 76, pp. 406–416, Jul. 2017.
- [36] W. C. Gu, G. H. Lv, H. Chen, G. L. Chen, W. R. Feng, and S. Z. Yang, “PEO protective coatings on inner surface of tubes,” *Surf. Coatings Technol.*, vol. 201, no. 15, pp. 6619–6622, Apr. 2007.
- [37] W. C. Gu, G. H. Lv, H. Chen, G. L. Chen, W. R. Feng, G. L. Zhang, and S. Z. Yang, “Preparation of ceramic coatings on inner surface of steel tubes using a combined technique of hot-dipping and plasma electrolytic oxidation,” *J. Alloys Compd.*, vol. 430, no. 1–2, pp. 308–312, Mar. 2007.



- [38] T. W. Clyne and S. C. Troughton, "A review of recent work on discharge characteristics during plasma electrolytic oxidation of various metals," *Int. Mater. Rev.*, vol. 64, no. 3, pp. 127–162, Apr. 2019.
- [39] W. Yang, Q. Li, C. Liu, J. Liang, Z. Peng, and B. Liu, "A comparative study of characterisation of plasma electrolytic oxidation coatings on carbon steel prepared from aluminate and silicate electrolytes," *Surf. Eng.*, vol. 34, no. 1, pp. 54–62, Jan. 2018.
- [40] Z. Zhao, M. Chen, C. You, W. Li, D. Tie, and H. Liu, "Effect of  $\alpha$ -Al<sub>2</sub>O<sub>3</sub> additive on the microstructure and properties of MAO coatings prepared on low carbon steel," *J. Mater. Res. Technol.*, 2020.
- [41] Y. Wang and Z. Jiang, "In situ formation of low friction ceramic coatings on carbon steel by plasma electrolytic oxidation in two types of electrolytes," *Appl. Surf. Sci.*, vol. 255, no. 12, pp. 6240–6243, Apr. 2009.
- [42] Y. Wang, Z. Jiang, Z. Yao, and H. Tang, "Microstructure and corrosion resistance of ceramic coating on carbon steel prepared by plasma electrolytic oxidation," *Surf. Coatings Technol.*, vol. 204, no. 11, pp. 1685–1688, Feb. 2010.
- [43] Y. Wang, Z. Jiang, and Z. Yao, "Preparation and properties of ceramic coating on Q235 carbon steel by plasma electrolytic oxidation," *Curr. Appl. Phys.*, vol. 9, no. 5, pp. 1067–1071, Sep. 2009.
- [44] S. A. Galedari, and M. M. Khoei "Characterization of oxide film formed on Ck45 steel by plasma electrolytic oxidation method," *Journal of Mechanical Research and Application*, vol. 4, no. 2, pp. 57-61, 2012.
- [45] L. Pezzato, K. Brunelli, P. Dolcet, and M. Dabalà, "Plasma electrolytic oxidation coating produced on 39NiCrMo3 steel," *Surf. Coatings Technol.*, vol. 307, pp. 73–80, Dec. 2016.
- [46] Y. Wang, Z. Jiang, and Z. Yao, "Microstructure, bonding strength and thermal shock resistance of ceramic coatings on steels prepared by plasma electrolytic oxidation," *Appl. Surf. Sci.*, vol. 256, no. 3, pp. 650–656, Nov. 2009.
- [47] M. Sowa and W. Simka, "Electrochemical Impedance and Polarization Corrosion Studies of Tantalum Surface Modified by DC Plasma Electrolytic Oxidation," *Materials (Basel)*, vol. 11, no. 4, p. 545, Apr. 2018.
- [48] M. Sowa and W. Simka, "Electrochemical impedance and polarization corrosion studies of tantalum surface modified by DC Plasma electrolytic oxidation," *Materials (Basel)*, vol. 11, no. 4, Apr. 2018.
- [49] X. Qi, H. Shang, B. Ma, R. Zhang, L. Guo, and B. Su, "Microstructure and Wear Properties of Micro Arc Oxidation Ceramic Coatings," *Materials (Basel)*, vol. 13, no. 4, p. 970, Feb. 2020.